Graded-Index Integrated Photonics

A Dissertation
Presented to the Faculty of the Graduate School
of Cornell University
in Partial Fulfillment of the Requirements for the Degree of
Doctor of Philosophy

by
Lucas Heitzmann Gabrielli
August 2012

© 2012 Lucas Heitzmann Gabrielli

Graded-Index Integrated Photonics

Lucas Heitzmann Gabrielli, Ph.D.

Cornell University 2012

Lead by the theory of Transformation Optics and developments in metamaterials, the field of complex structures is growing in importance in the scientific community. In optics, those concepts add design flexibility to graded-index devices, but fabrication of high refractive index contrasts at the nanometer scale is still challenging. In this work we propose three fabrication techniques for high contrast graded-index integrated photonics using only dielectric materials. By avoiding metals and resonant nano-structures we are capable of broad wavelength ranges of operation. Using our fabrication platforms we show how graded-index media can be used to improve existing nanophotonic devices and enable new features in optical systems. Three devices are demonstrated: first, an invisibility cloak that hides a region of space from any external observer. It is implemented with the help of effective material theory and it is composed of nanometer-size silicon pillars. Second, we show that by using a graded-index Luneburg lens to mediate the coupling between optical fibers and highly confined channel waveguides, we can decrease the sensitivity to misalignment in fiber-to-chip couplers. Finally, an optimization algorithm tailored to Transformation Optics in dielectric-only graded media is developed and used to design a multimode waveguide bend with minimal mode conversion. Fabricated via grayscale electron beam lithography, this demonstration enables the utilization of multimode waveguides for integrated photonics and leverages their advantages over the single mode ones, such as lower propagation loss and higher numerical aperture, without the issue of modal dispersion. Low modal conversion also points towards the possibility of mode multiplexing in future optical interconnects, a path to increase the bandwidth of conventional wavelength-multiplexed systems by folds.

Biographical Sketch

Lucas Gabrielli was raised in São Paulo, Brazil, where he graduated in 2001 from Colégio Etapa. At Instituto Tecnológico de Aeronáutica (ITA) in São José dos Campos, he majored in Electronics Engineering and received his Bachelor's degree *Magna Cum Laude* in 2006. While working at the Wenher von Braun Research Center in Campinas, Brazil, he decided to continue his education at Universidade Estadual de Campinas (UNICAMP) in Professor Hugo Figueroa's group, where he obtained his Master's degree in Electrical Engineering in 2009 for his work on fiber optical parametric amplification. After that, Lucas joined Professor Michal Lipson's research group at Cornell University in New York, USA, as a Ph.D. candidate in the field of integrated photonics. In 2012 he obtained his doctorate degree and in the near future Lucas will be working as a post-doctoral researcher at UNICAMP, with plans to apply for a faculty position and continue his academic career.

This is dedicated to my family, who has always given me the support to pursue my dreams,

to my fiancée, who gives me the strength and the will to reach beyond my limits,

to my niece, whose birth became my anchor home.

Acknowledgements

First of all I would like to thank my advisor and mentor, Professor Michal Lipson. Her unwavering dedication and inspiration make her an invaluable model for me both professionally and personally. Aiming high and overcoming obstacles have a complete new meaning to me after my experience at the Cornell Nanophotonics Group, all thanks to her.

I also thank my committee members, Professors Cliff Pollock and Alex Gaeta, for the insights and advices in keeping in mind the broader picture and fundamental ideas, when it is very easy to dive deep in my own field and forget the relations with other areas.

The great time I had in our group would have definitely not been the same without Carl, always available to help me with anything from theory to experiment, or any related or not-so-related problems. It is hard to thank him enough, and impossible to image the group without his support.

I must also thank all the great friends I've met in the group. All the (scientific) discussions and sharing of (failed) experiences were fundamental for me to get this far. That, and caffeine—so I also acknowledge our well maintained espresso maker. From our group, I want to thank in particular Jaime, our fabrication guru, who showed me the ways of the clean room and jump-started my work in a field I had no experience whatsoever.

I also want to acknowledge the collaborators whom I had the pleasure to learn from: Professor Ulf Leonhardt, who taught me the theory of Transformation Optics, a fundamental design tool throughout this work; and Professor Steven Johnson, whose insights and knowledge are an inspiration for me to always look at the fundamental science behind the engineering.

Finally I would like to acknowledge the support of Cornell's Center for Nanoscale Systems (CNS), funded by the National Science Foundation. This work was performed in part at the Cornell Nanoscale Facility, a member of the National Nanotechnology Infrastructure Network, which is supported by the National Science Foundation. This work has been partially supported by the AFOSR MURI for Complex and Robust On-chip Nanophotonics (Dr. Gernot Pomrenke), grant number FA9550-09-1-0704.

Table of Contents

List of Figures

List of Tables

List of Abbreviations

AFM	atomic force microscope
BOE	buffered oxide etch
CMOS	complementary metal-oxide-semiconductor
DBR	distributed Bragg reflector
DT	dwell time
DUV	deep ultra-violet
FDTD	finite-difference time-domain
FIB	focused ion beam
FWHM	full width at half maximum
GRIN	graded-index
ICP	inductively coupled plasma
IPA	isopropyl alcohol
PEC	proximity effect correction
PECVD	plasma-enhanced chemical vapor deposition
PMMA	poly(metil methacrylate)
PSF	point spread function
RF	radio frequencies
RIE	reactive ion etching
RMS	root mean square
SEM	scanning electron microscope
SOI	silicon-on-oxide
TE	transverse electric
TM	transverse magnetic
TO	Transformation Optics

1 Introduction

Within the field of electromagnetism, the use of homogeneous media by far dominates the design and analysis of devices. The decomposition of the fields in plane waves in the bulk, either travelling or evanescent, associated with the boundary conditions at the interfaces between different materials gives not only a complete, but also intuitive description of the electromagnetic fields in homogeneous media. From the understanding of the field behavior in simple problems, such as transmission and reflection at parallel interfaces, we are able to predict to a great extent the result of more complex structures, such as

---

[1] This dissertation uses materials with permissions from:

L. H. Gabrielli, J. Cardenas, C. B. Poitras, and M. Lipson, "Silicon nanostructure cloak operating at optical frequencies," *Nature Photonics*, vol. 3, no. 8, pp. 461-463, Jul. 2009, DOI: 10.1038/nphoton.2009.117.

L. H. Gabrielli and M. Lipson, "Transformation optics on a silicon platform," *Journal of Optics*, vol. 13, no. 2, p. 024010, Feb. 2011, DOI: 10.1088/2040-8978/13/2/024010.

L. H. Gabrielli and M. Lipson, "Integrated Luneburg lens via ultra-strong index gradient on silicon," *Optics Express*, vol. 19, no. 21, p. 20122, Sep. 2011, DOI: 10.1364/OE.19.020122.

tightly confined slot waveguides or photonic bandgap mirrors. The advantages of working with simple media and those insights are clear in the myriad of advances we have made in all areas dealing with electromagnetism, from antennas to transmission lines and integrated electronics.

Nevertheless, if constraining our design space to homogeneous media allows us to benefit from useful insights and readily available analysis tools, it also separates us form the rich and still quite unexplored universe of solutions within inhomogeneous media. Intuitively, the addition of this degree of freedom should lead to improvements in existing devices and discovery of new features impossible to be achieved otherwise.

Examples of designs using non-homogeneous media, although few, do exist in both the scientific literature and commercial devices, most notably in graded-index (GRIN) optical fibers [1–6] and lenses [7–10]. It is understandable why GRIN media is not often employed in other electromagnetic devices for two main reasons: first, the design and analysis of inhomogeneous materials is more difficult, more computationally expensive, and less intuitive than their homogeneous counterparts; and second, the fabrication of such materials generally requires more complex processes, which are usually more expensive as well, when at all feasible.

The successful development of GRIN fibers and rod lenses illustrates the points above. The use of inhomogeneous materials led to improvements of existing devices—as in the case with optical fibers, where lower dispersion is possible with quasi-parabolic core profiles [2]—and was only possible because of advances in fiber fabrication techniques [3, 6]. The new fabrication methods allowed for the control of the refractive index of fibers or rod

lenses as a function of their radial position, which means that the designed GRIN media must axisymmetric. This geometrical constraint, coupled to the fact that the refractive indices in glass fibers vary less than a few percent at most, enabled the analysis of these media and successful design and optimization of the fibers and lenses.

Without further advances in fabrication capabilities or theoretical tools to treat inhomogeneous media, interest declined in the field of GRIN devices. However, in 1996 Ward and Pendry rediscovered the equivalency of geometry and media in Maxwell's equations [11] (previously found in [12, 13]), and proposed that it could be used in numerical algorithms to deal with complex geometries by transforming the coordinate system into a simpler one to solve and using a corresponding renormalization of the constitutive material parameters. A decade latter the strength of this theory, now known as Transformation Optics (TO), would be brought about by several authors [14–17], and would be used to design and analyse a number of novel devices, many impossible to be obtained without the use of complex inhomogeneous media. Among those, the optical invisibility cloak is probably the most famous and the one that received most attention from both the scientific community and general media due to the its vast application possibilities, such as camouflage in military environments.

If on the theoretical side TO gave a new breath to the design of GRIN devices, it would have been short-lived had developments in fabrication not allowed the demonstration of artificially structured materials (or metamaterials) around the same time [18–22]. Because the fabrication of GRIN metamaterials is still challenging today in optical and infrared frequencies the first demonstrations of GRIN devices were achieved in longer wavelengths, namely radio frequencies (RF) and microwaves, where length scales are several orders of magnitude larger,

enabling the realization of precisely engineered material properties, including inhomogeneity and anisotropy.

1.1 Objective and Dissertation Structure

In this context, our goal is to demonstrate the benefits of GRIN devices in the field of integrated optics and, at the same time, develop a viable platform for fabrication and integration of such devices in future generations of nanophotonic chips. Because of the scale of the wavelengths in optical fields, the availability of GRIN metamaterials is scarce, thus we chose different fabrication routes to create effectively inhomogeneous media. Our techniques provide less design freedom than arbitrary metamaterials, which creates additional constraints to the TO design process, but it allows for the demonstration and analysis of high-contrast GRIN devices that can be integrated with the current silicon platform.

Initially, a review of the general TO theory will be presented in chapter 2. We will show that the geometry of space and the constitutive parameters of material have the same effect on electromagnetic waves, therefore we can freely replace one for the other. In other words, by carefully tailoring material parameters, we are able to create or correct geometrical distortions for electromagnetic waves and control their flow at will. Latter, from section 2.3 forward, we will introduce our material system and fabrication methods, defining the additional constraints in our GRIN device designs.

The following three chapters will demonstrate the use of our fabrication platforms via different GRIN devices. First we will demonstrate the cloaking effect in the optical domain in chapter 3 by rendering a region of space undetectable to an external observer, where any

object can be safely hidden, regardless of its material composition. Following that, chapter 4, will show an example of integrated GRIN lens used to improve the coupling robustness of integrated channel waveguides with silicon to optical fibers. This aberration-free and comma-free lens, called a Luneburg lens, decreases the alignment sensitivity between fiber and waveguide, a key characteristic for mass production and commercialization of packaged integrated photonic chips. The last demonstrated device, in chapter 5, is an integrated multimode waveguide bend with minimal mode conversion. This bend allows for compact routing of waveguides with both wavelength- and mode- multiplexed channels, increasing their transmitted data bandwidth by folds. Finally, in chapter 6 we will draw the main conclusions from the achieved results and present future directions and opportunities emerging from this work.

2 Transformation Optics

The theory of TO is a powerful design tool for GRIN devices, because it allows us to freely mold the flow of radiation by deforming a virtual space where it propagates. Once the desired deformation (or, more precisely, coordinate system transformation) is found, we are able to translate it into an inhomogeneous material, which will give the same radiation pattern in real space as in the deformed virtual space [14–17, 23–25].

The idea that the geometry of space and media are closely related is not new [12, 13]. We know that the measure of distance in geometrical optics is weighted by the refractive index of the materials, a fundamental concept in Fermat's Principle, for example. When we look at it in a more fundamental level, the role of materials is found explicitly in the constitutive relations between the electric and magnetic fields, $\vec{E}$ and $\vec{H}$, and the flux densities, $\vec{D}$ and $\vec{B}$, via the permittivity and permeability tensors $\bar{\varepsilon}$ and $\bar{\mu}$ of the medium.

$$\vec{D} = \varepsilon_0 \bar{\varepsilon} \vec{E}$$

$$\vec{B} = \mu_0 \bar{\mu} \vec{H} \tag{2.1}$$

It is less obvious, at first glance, to notice the effects of space geometry (or, more generally, space-time geometry, although we will not discuss time transformations or relativity effects is this work), but looking at Maxwell's equations we find them included in all differential operators. The definitions of curl and divergence take into account the coordinate system to which the vectors belong, a fact reflected in the usual definitions of those operators for Cartesian, cylindrical, and spherical coordinates.

$$\begin{aligned} \nabla \cdot \vec{D} &= \rho & \nabla \times \vec{E} &= -\frac{\partial \vec{B}}{\partial t} \\ \nabla \cdot \vec{B} &= 0 & \nabla \times \vec{H} &= \frac{\partial \vec{D}}{\partial t} + \vec{j} \end{aligned} \tag{2.2}$$

The interplay between the two, geometry and medium, can be found by rewriting empty space Maxwell's equations (2.2) in arbitrary coordinates and comparing it to macroscopic Maxwell's equations in conventional Cartesian coordinates [24, 25]. Because these two sets of equations have the same form, we can freely interpret a Cartesian space filled with some material as empty curved space and vice-versa, i.e., we can design a device, for example a bend, by bending a virtual empty space, where radiation naturally propagates in a curve, and not in straight lines, but then interpret the equations governing the bent space as equations for real Cartesian space embedded in some inhomogeneous material. In the end we have the recipe for a dielectric medium that bends radiation, as would a waveguide, but, as we will see, without relying on interface effects, such as total internal reflection.

The following section will present a formal derivation of the equivalency between media and geometry in Maxwell's equations following [24, 25]. A more detailed and thorough derivation can be found in those references. Latter we will discuss the feasibility of this theory and how it can be employed in the design of electromagnetic devices with the help of metamaterials. From section 2.3 onwards we will introduce the capabilities and limitations found in the optical domain and the constraints it introduces in the general TO design.

2.1 Theoretical Derivation

Using a tensor notation with Einstein's summation and range conventions, Maxwell's equations in empty space and arbitrary geometry read [24, 25]:

$$\begin{aligned} \left(\sqrt{g}g^{ij}E_j\right)_{,i} &= \sqrt{g}\frac{\rho}{\varepsilon_0} & [ijk]E_{k,j} &= -\frac{\partial}{\partial t}\left(\pm\sqrt{g}g^{ij}B_j\right) \\ \left(\sqrt{g}g^{ij}B_j\right)_{,i} &= 0 & [ijk]B_{k,j} &= \mu_0\varepsilon_0\frac{\partial}{\partial t}\left(\pm\sqrt{g}g^{ij}E_j\right) + \mu_0\sqrt{g}j^i \end{aligned} \tag{2.3}$$

The comma in the subscript indicates the differentiation of a vector component ${V^j}_{,i} = \frac{\partial V^j}{\partial x^i}$, whereas the permutation symbol $[ijk]$ is defined as $+1$ for even permutations of 123, -1 for odd permutations, and 0 otherwise; g^{ij} is the inverse metric tensor of the coordinate system, and $g = \det g_{ij}$. The sign $+$ $(-)$ is chosen for a right-hand (left-hand) coordinate system.

Now we write the macroscopic version of Maxwell's equations in right-handed Cartesian coordinates:

$$\begin{aligned} {D^i}_{,i} &= \rho & [ijk]E_{k,j} &= -\frac{\partial B^i}{\partial t} \\ {B^i}_{,i} &= 0 & [ijk]H_{k,j} &= \frac{\partial D^i}{\partial t} + j^i \end{aligned} \tag{2.4}$$

Equations (2.3) can be written in the same form as (2.4) if we rescale the charges and current densities and use the constitutive relations:

$$D^i = \pm\varepsilon_0\sqrt{g}g^{ij}E_j$$

$$B^i = \pm\mu_0\sqrt{g}g^{ij}H_j \tag{2.5}$$

which are equivalent to (2.1) if we equate the material parameters of the medium to:

$$\varepsilon^{ij} = \mu^{ij} = \pm\sqrt{g}g^{ij} \tag{2.6}$$

This equation explicitly translates a curved space geometry defined by its metric tensor into the permittivity and permeability tensors of an impedance-matched medium in Cartesian coordinates (by impedance-matched we mean that $\bar{\varepsilon} = \bar{\mu}$, so that the impedance of the material is the same as free-space). The same can be done between two curved spaces, but that is not necessary for the applications intended.

The consequence of the equivalence between geometry and media, and the reason why TO is such a powerful design tool, is that it gives us freedom to tailor the flow of electromagnetic radiation via spacial deformations. We can deform the geometry of space by contracting or expanding it, introducing bends, or even tearing it apart, and the electromagnetic waves will propagate according to those same deformations. Then we can replicate this deformed geometry in Cartesian space by filling it with a medium described by (2.6), so that the waves are still governed by the same set of equations, thus propagating exactly as they would in the deformed space, as illustrated in figure 1, but now in real Cartesian space.

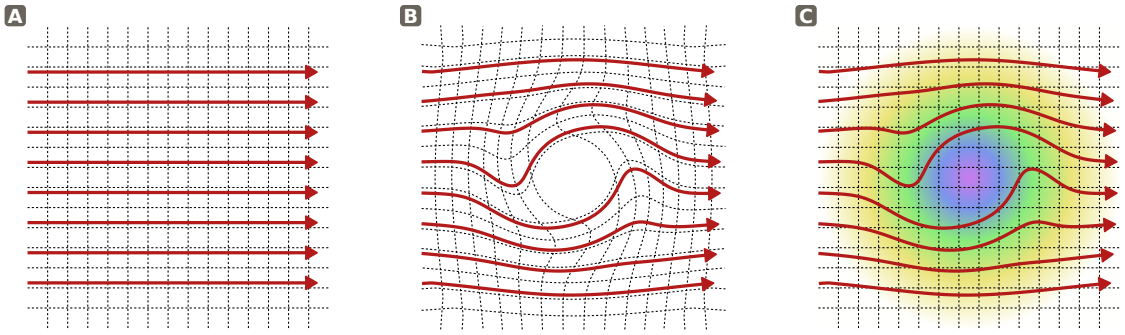

Figure 1 Medium and geometry interplay in TO. **(a)** In empty space plane waves will propagate in straight lines, represented by the red arrows (power flux). **(b)** When the geometry of space is deformed, the electromagnetic waves will follow that same deformation—we can think in terms of light rays following the deformed grid, or geodesics, of the coordinate system. **(c)** Using media prescribed by (2.6), we can remove the deformation of space while preserving the wave propagation characteristics of the deformed geometry.

In essence, the design via TO is done by defining and optimizing a coordinate transformation that maps Cartesian space (or possibly other curved geometries) into the desired virtual space. Once this transformation is found, (2.6) produces a material parameter map that must be implemented to create the virtual geometry. It is useful to gather some intuition on the coordinate transformation and what material parameters it might produce in order to accelerate and guide the design process. If we look at 2-dimensional coordinate transformations and their "grid" representations (by drawing the geodesics of the coordinate systems, such as in figure 1) we will find that, in broad terms, the magnitude of the material parameters is inversely proportional to the local scaling of the transformation, that is, in regions where the grid cells are squeezed we expect higher values for the material parameters, and the opposite for expanded areas. Hence if we compress a finite area into a point so that light converges into it, we expect the parameters at this point to diverge to infinity. We will also find that the amount of anisotropy in the tensors is related to the distortion

of the "grid" cells, i.e., how tilted or irregular the originally square cells become after the transformation. These two simple rules of thumb help give a good idea of what to expect from the transformation media parameters, given the geometrical deformation.

2.2 Metamaterials

The power and freedom allowed by TO does not come for free. The material prescription (2.6) indicates that in the general case the constitutive parameters of the transformation medium are not only inhomogeneous, but also anisotropic, and in extreme cases, can reach unnatural and singular values. The extreme difficulty in creating such media with conventional materials is probably the main reason why the theory of TO remained unused from its first appearances [12, 13] to 2006 [14, 16].

However, around the mid 1990's the idea of metamaterials was starting to come into shape [18, 26], inspired, at first, by the quest for materials with simultaneously negative permittivity and permeability [27–34]. In essence, metamaterials are artificially structured materials with tailored electromagnetic responses. The structures embedded in the material have dimensions usually smaller then the wavelength of operation, but not so small as to fall into the effective material regime, and show resonances around that same wavelength. The classical example of resonant structured metamaterial is the split-ring resonator [26, 28, 29], illustrated in figure 2. The presence of resonances, both electric and magnetic, gives the metamaterial an extended range of possible constitutive parameters, all the way from very large values down to negative, passing of course through effective zero electric and magnetic responses.

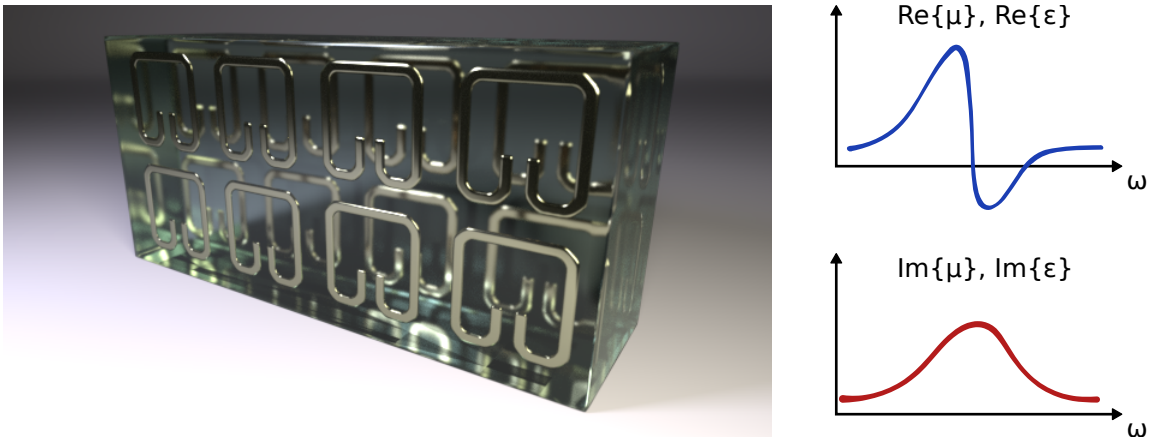

Figure 2 Illustration of metamaterial composed of an array of split ring resonators. These structures, smaller than the wavelength of operation, are responsible for the resonant electromagnetic responses of the metamaterial and its tailored effective permittivity and permeability constants. The plots on the right illustrate the expected material response around resonances. Note that losses can become a problem in resonant metamaterials.

This unprecedented design freedom gave birth to a multitude of new ideas in the field of applied electromagnetism, including lumped elements for optical circuits [35–38] and super-lensing [39–43]. But more importantly for TO, it provided the key to implementing transformation media, via careful tailoring the embedded metamaterial structures to form the required inhomogeneous designs [19, 44]. The results from the symbiotic relation between TO and metamaterials are clear in the many examples of innovative devices demonstrated in the past years [44–47].

2.3 Transformation Optics in Optical Frequencies

From the many applications of TO, invisibility cloaks are certainly the most cited and investigated, and, although useful in microwave frequencies for security and communication applications, the idea of cloaking is specially attractive at optical wavelengths. The same

also applies to other devices, such as super-lenses or broadband concentrators with ultra-high numerical aperture, and as such, there is special interest in employing TO optical frequencies.

On the other hand, classic metamaterial fabrication is very challenging at such small scales, where conventional techniques for integrated photonics are tailored to homogeneous films and planar structures in general. It was not until 2008 that a successful demonstration of metamaterials in the optical domain was obtained [48], and even then, the material is still homogeneous and lossy, due to the nature of metals at optical frequencies. While advances in 3-dimensional patterning show promising results for the future of optical metamaterials [49–51], the achievable length scales are not yet small enough to provide the required flexibility for media fabrication with a wide range of parameters in terms of inhomogeneity and anisotropy [52].

With those limitations in mind, additional constraints must be introduced in the TO design to avoid impossible material requirements. These constraints are directly related to current optical fabrication capabilities, in special the difficulty in controllably creating inhomogeneous films via deposition, diffusion or implantation. Still, it is possible to fabricate significantly high-contrast GRIN media in optical frequencies without the need of resonant metamaterials. The fabrication platforms we developed use either material homogenization or waveguide dispersion to produce effective material gradients, allowing us to demonstrate TO in near infrared wavelengths.

In the following subsections we will explain the constrains and approximations necessary to bring TO to optical frequencies, and later, in section 2.4, the details of the fabrication platforms will be shown.

2.3.1 Planar Devices

The first requirement of our fabrication platforms is that the design must be 2-dimensional. Conventional micro- and nano-fabrication technologies are based on deposition and patterning of thin films, so it natural that planar devices are more readily achievable than 3-dimensional structures. Although in some cases 3-dimensional structures would be preferred (such as the case for a perfect invisibility cloak), in many areas—and specially for applications in optical interconnects—planar devices provide sufficient degrees of freedom to solve the design problem at hand, as we will see in the following chapters.

By using TO in 2 dimensions (we define $\hat{z}$ as the direction perpendicular to the design plane and, consequently, $\frac{\partial}{\partial z} = 0$), the material parameter tensors (2.6) will have the forms:

$$\bar{\varepsilon} = \begin{bmatrix} \varepsilon_{xx} & \varepsilon_{xy} & 0 \\ \varepsilon_{yx} & \varepsilon_{yy} & 0 \\ 0 & 0 & \varepsilon_{zz} \end{bmatrix} \qquad \bar{\mu} = \begin{bmatrix} \mu_{xx} & \mu_{xy} & 0 \\ \mu_{yx} & \mu_{yy} & 0 \\ 0 & 0 & \mu_{zz} \end{bmatrix} \tag{2.7}$$

In such case, the solutions to the 2-dimensional Maxwell equations can be divided in 2 classes: transverse electric (TE) and transverse magnetic (TM). In the former the electric field is perpendicular to the propagation plane, and in the latter the magnetic field.

As will become clear later on, by employing planar TO design we are left with the third dimension as a degree of freedom in the actual implementation of the designed 2-dimensional transformation media into a 3-dimensional device.

2.3.2 Slowly Varying Parameters

As showed in section 2.1, TO designs are impedance-matched to empty-space. If on the one hand this means that the devices will present no reflections, on the other it also means that the transformation media will require equal electric and magnetic responses. For metamaterials this can be achieved by designing structures with both magnetic and electric resonances, such as double split ring resonator.

In optics however, because fabrication of such nano-structures is not yet an option and natural materials have no magnetic response, a second requirement rises, which is that the constitutive tensors vary slowly compared to the wavelength scale across the medium. In this case, the tensors can be approximately commuted with the curl operator in the wave equation, such that we are left only with the product $\bar{n}^2 = \bar{\mu} \cdot \bar{\varepsilon}$, i.e., the media can be described by a refractive index tensor, which is a function of the position on the propagation plane $\bar{n}(x, y)$.

Concretely, that means that both electric and magnetic responses are absorbed by a single parameter, which due to the lack of magnetic materials at optical frequencies, will be the electric permittivity, while the permeability will remain 1. As a result, the devices will no longer be necessarily impedance matched to their surrounding, so reflections at the boundaries might occur. These, however, can be addressed in the device design and do not represent a major limitation.

2.3.3 Isotropy and Index Range

The final requirement from our platforms concerns the refractive indices we are capable of

obtaining. Without the enhancements from resonant structures, we employ homogenization and wave guiding as strategies to obtain GRIN media. Consequently, the range of indices we can achieve are necessarily bound by the highest and lowest bulk material indices we have available for fabrication. Nevertheless, avoiding resonant metamaterials also results in a valuable benefit: the devices have inherently broad wavelength bandwidth. The wavelengths of operation will generally be limited by material dispersion, homogenization condition, or the slowly varying parameters approximation discussed before, all of which affect performance much slower than resonances.

Additionally, we chose to optimize our TO designs to generate isotropic or *quasi*-isotropic materials only. Even though anisotropic materials are available in optics, such as SiC, controlling both the index gradient and its anisotropy would increase the complexity of fabrication by many folds. As we mentioned previously, the anisotropy of the material will be related to the amount of distortion in the transformation. To be more exact, transformations with no anisotropy are angle-preserving transformations, which are called conformal maps [14, 25]. These transformations can be represented by an analytic function in the complex plane and are very useful in the design of isotropic transformation media. If conformal maps cannot be found for the desired transformation, it is common to use numerical optimization algorithms to find *quasi*-conformal transformations with minimized residual anisotropy [53]. Figure 3 shows an example of application of such an algorithm. Both transformations have the same external boundary shape, but the interior of the one on figure 3a is created simply by interpolating those boundaries, while in figure 3b the interior is optimized to minimize anisotropy.

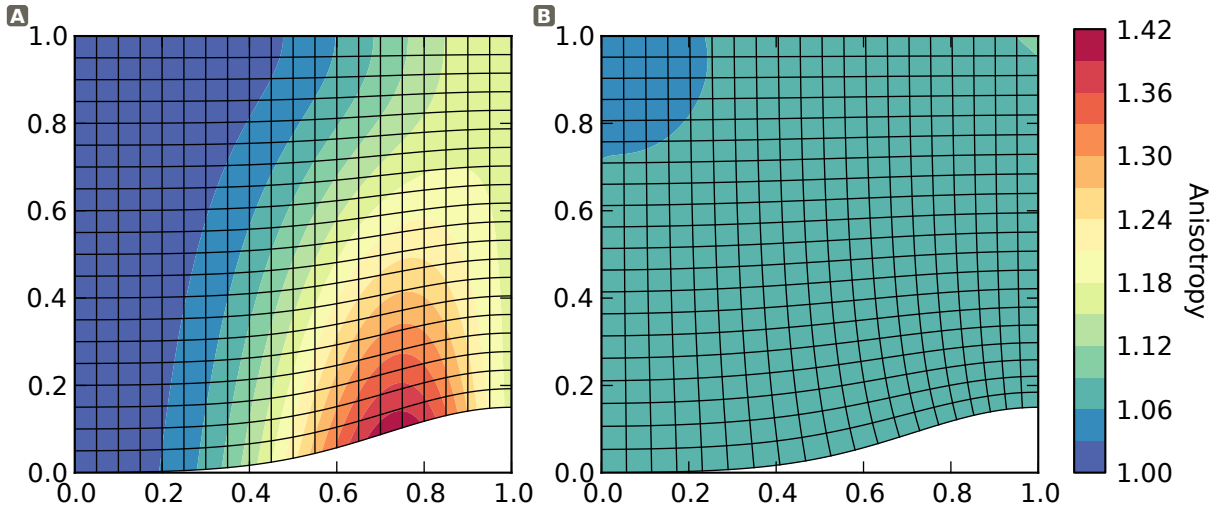

Figure 3 Transformation optimization to minimize anisotropy. The contours show a measure of local anisotropy defined as the ratio between the maximal and minimal refractive indices along the principal axis of the medium [53]. Both transformations map a square Cartesian region to an area with a deformed bottom edge, but in **(a)** the interior of the transformation is defined as a direct interpolation of the boundaries, while in **(b)** the transformation is optimized to be *quasi*-conformal, leading to minimal residual anisotropy of less than 10%.

2.4 Fabrication Platforms

Because we design the transformation medium in 2 dimensions and the material parameters vary slowly in the propagation plane, we can decouple the geometry in the perpendicular direction $\hat{z}$ from the in-plane propagation. Thus, to confine the field in this direction, we use a dielectric slab waveguide, as shown in figure 4a, which we can freely tailor to produce the required GRIN map in the propagation plane.

In this plane it is no longer the absolute material refractive index that will control the wave propagation, but the effective propagation index $n_{\text{eff}} = \frac{k}{k_0}$ of the dielectric slab structure, where k is the propagation constant in the slab, and k_0 the free-space wavenumber. From there, it becomes quite clear that two parameters are available to control the propagation index: material refractive indices and slab dimensions. The graph in figure 4b

shows a contour plot of the propagation index of the slab versus both those parameters. We can see the range of possible indices for a slab in vacuum with core material index varying from 1 to 2.5 and thickness varying from 0 to $\frac{\lambda}{2}$ for its fundamental TE mode, λ being the free-space operation wavelength. (Note that the fields for the TE and TM modes in a slab waveguide will almost match the field for the TM and TE propagation problems in 2-dimensions, respectively, as defined in subsection 2.3.1).

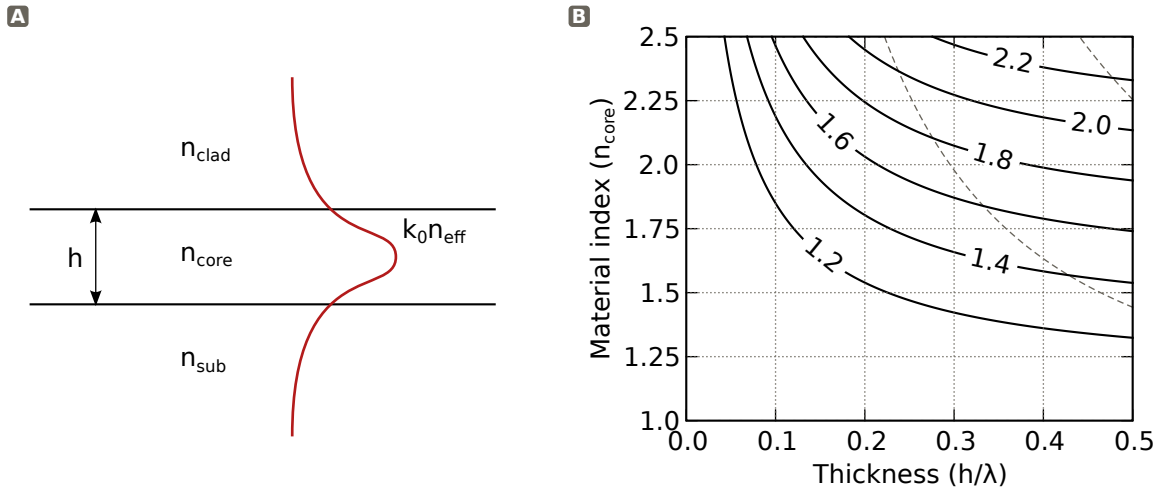

Figure 4 GRIN media via effective slab index. **(a)** The 1-dimensional slab allows the control of the guided index through its dimensions and materials. **(b)** Effective guided indices for the fundamental TE mode achievable in a slab with $n_{\text{clad}} = n_{\text{sub}} = 1$ as a function of its core thickness and index. Dashed lines show the cutoff for the second and third order TE modes.

Regardless of the control parameter we use, the limits in the effective refractive index are set by the material indices of the slab. The greater our effective index range, the less constrained our TO design is, which means more space efficient devices, i.e., same functionality in a smaller footprint, since the refractive index is approximately proportional to the amount of squeezing in the transformation. It is thus beneficial to use materials for core and

cladding with strong index contrast.

That being the case, we decided to work with crystalline silicon as our core material and SiO_2 (or air) for cladding. The refractive index of silicon in the near infrared region is approximately 3.48, whereas SiO_2 and air have indices around 1.44 and 1.0, respectively. The provided material index contrast is very strong: the core has at least 2.4 times higher index than the surrounding material. Another great advantage of using silicon is that the fabrication processes in both the complementary metal-oxide-semiconductor (CMOS) and nanophotonics industries are quite mature, an invaluable benefit since we expect fabrication to be one of the limiting factors in our designs. Last, using a CMOS-compatible process allows immediate integration of our TO devices with existing nanophotonic systems, the main candidates for future ultra-high data rate interconnects.

We use silicon-on-oxide (SOI) wafers as fabrication substrate with a 3 µm thick buried SiO_2 layer and a 500 nm top silicon layer serving as our slab core. As we mentioned earlier, it is possible to control the effective propagation index of this slab by the material indices and slab dimensions. We explored and demonstrated both alternatives, each with its strengths and drawbacks. In the following subsections we will describe in detail each of the two fabrication platforms.

2.4.1 Effective Material Theory

The first way to create the refractive map required from TO via the effective slab index is to use the material of the slab core [54]. Using a numerical or analytical 1-dimensional slab solver we can translate the transformation medium refractive index map into the correspond-

ing slab core material index map, given the slab thickness and surrounding materials.

It might be possible to change the refractive index of the actual material in the slab core of our guiding structure via, for instance, implantation and diffusion of dopants, as is the case in GRIN fibers. Another option would be to use SiON films with varying contents of oxygen and nitride [55–57]. However, both options would make it very hard to control the index of the deposited film in the plane, apart from providing only a relatively smaller contrast than Si on SiO_2.

Alternatively, we chose to work with effective material theory, which states that a media composed of a mixture of materials with small enough granularity (compared to the wavelength) can be treated macroscopically as an homogeneous medium with refractive index given by an average between the indices of the composing materials [58]. Thus, by patterning the silicon layer with nano-scale structures using electron beam lithography we are able to create a homogenized core material with refractive index varying between 1.45 and 3.48 (for SiO_2 and Si), or 1 and 3.48 (for air and silicon). The exact index will depend on the structure of the mixture. Since we use conventional lithography and anisotropic plasma etching, the patterned slab core will be composed of pillars of Si in an air or SiO_2 matrix, or holes in the Si layer filled with air or SiO_2, depending on the volumetric fraction of silicon in the desired mixture.

This vertical pillar structures determine the kind of averaging used for the homogenized refractive index. For each slab polarization, we will have the effective material permittivities [58]:

$$\varepsilon_{\mathrm{TM}} = \sum_{m=1}^{M} \xi_m \varepsilon_m$$
$$\varepsilon_{\mathrm{TE}} = \left(\sum_{m=1}^{M} \frac{\xi_m}{\varepsilon_m} \right)^{-1} \tag{2.8}$$

where ξ_m is the volumetric fraction of the m-th material ($\sum_m \xi_m = 1$). These equations allow us to transform the slab core index $n_{\mathrm{core}}(x, y)$ into a volumetric fraction map of Si in SiO_2 or air $\xi_{\mathrm{Si}}(x, y) \in [0, 1]$. The volumetric fraction is a continuous function defined over a continuous (or very finely discretized) domain, but our final pillar structures have dimensions around tens of nanometers and each pillar or gap between pillars is made of a single material (have volumetric fraction either 1 or 0). Hence the need to created a quantized version of the volumetric fraction map with proper domain.

This is accomplished by sampling ξ_{Si} over a grid on the device plane where each cell has a dimensions $d \times d$ (which will become the lateral dimensions of the pillars) and quantizing the resulting map using a dithering algorithm [59]. Dithering is a very common algorithm in image processing to quantize color levels, an analogous process to what we need: quantizing a grayscale map defined in the $[0, 1]$ interval into two levels, 0 and 1, that will represent grid cells (or pillars) made entirely of Si and SiO_2 or air, respectively. The algorithm, demonstrated in figure 5, minimizes the error in the quantization process. Therefore, the local density of silicon pillars (or holes into the silicon layer) will directly define the effective index of that area in the slab core, reproducing the desired material index map $n_{\mathrm{core}}(x, y)$. The scanning electron microscope (SEM) image in figures 5c and d show the actual silicon pillars fabricated using this platform. The device in the images is a invisibility cloak, which will be presented latter in chapter 3.

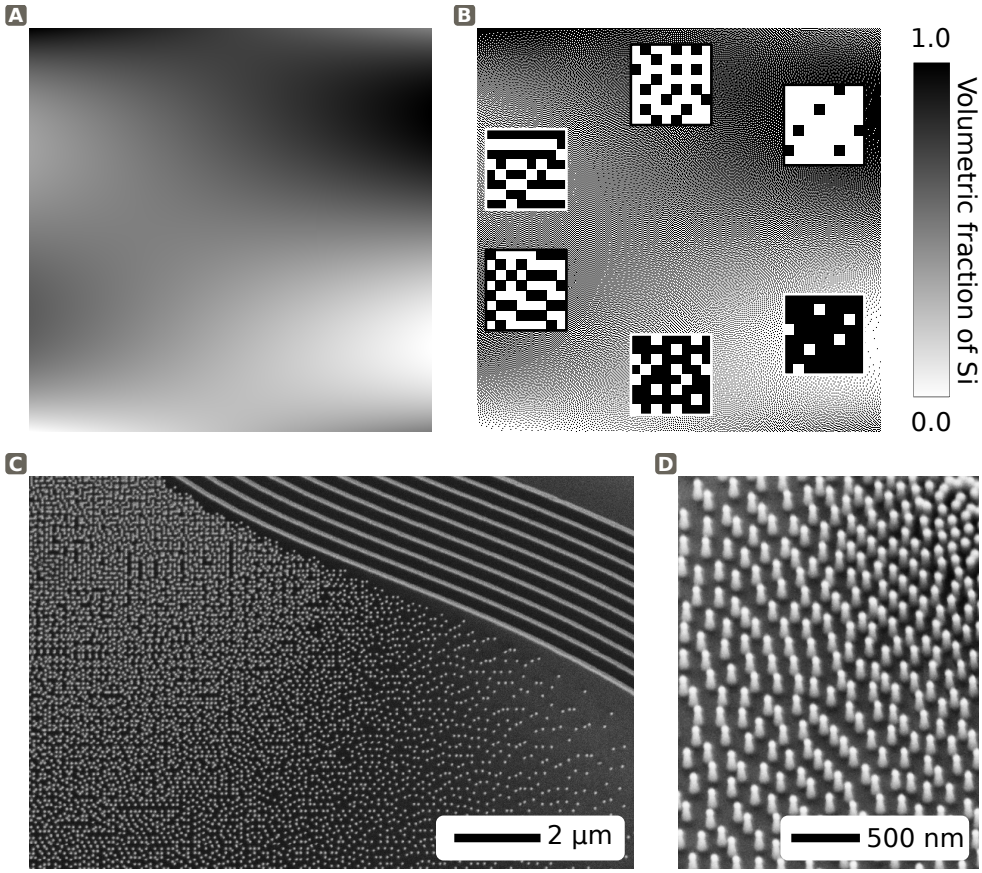

Figure 5 Dithering and effective material GRIN medium. The grayscale map representing the volumetric fraction of silicon **(a)** is dithered into a black and white map **(b)**, representing the positions of the silicon pillars and holes that result in an effective material. **(c)** SEM image showing an example of GRIN medium fabricated in silicon using this platform. The density of silicon pillars is proportional to the local effective material index. A Bragg reflector is also visible in the upper right corner, but it is not part of the transformation medium. **(d)** Close-up view of the silicon pillars that form the effective material. In this device the pillars have lateral dimensions of approximately 50 nm.

This platform for GRIN medium presents two benefits: high achievable contrast between highest and lowest effective slab indices, and use of conventional nano-fabrication techniques. The index contrast obtainable in the effective material slab can easily reach above 2, as table 1 shows, specially for a thick core. The fabrication of the nano-pillars is

accomplished by high-resolution electron beam lithography and highly anisotropic plasma etching, both techniques commonly used in nano-photonics and CMOS industries.

Table 1 Effective index ranges for slabs of different core thicknesses, polarizations, and cladding materials (SiO_2 substrate) at 1.55 µm wavelength.

Thickness (nm)	**TM**		**TE**	
	SiO_2	**air**	**SiO_2**	**air**
500	1.44 – 3.16	1.59 – 3.15	1.44 – 3.28	1.54 – 3.27
250	1.44 – 2.30	1.90 – 2.18	1.44 – 2.94	1.67 – 2.93

Nevertheless, due to the reduced dimensions of the pillars and holes and, more importantly, the different densities of these structures along the substrate, uniform etching of the devices is challenging. Regions formed mostly by sparse silicon pillars will etch much faster than region where the dithering process results in a few small holes on the silicon layer. Depending on the required contrast of the transformation medium, single step lithography and etching might not be at all possible, even with the help of a hard etching mask, specially for thicker films, where the best contrast is found. Nevertheless, further developments in nano-fabrication should continue improving the resolution and etching characteristics of thin films, enabling even smaller features and higher effective index contrast in a single device.

The second drawback of this platform is the resulting light scattering due to the discrete nature of the nano-pillars. This issue is more fundamental, because, although reduction of the pillar dimensions do decrease the scattering cross-section of the mixed medium, as

long as the discrete structures exist, they will necessarily contribute to scattering, which in turn becomes either loss or noise depending on the device.

2.4.2 Grayscale Patterning

We developed our second fabrication platform to tackle the fundamental issue in the previous one: losses due to light scattering. The idea behind this solution is to use the thickness of the guiding slab (figure 4) to define the effective propagation index [8–10, 60, 61]. By solving the inverse slab problem, i.e., finding the thickness that will result in the desired propagation constant, we convert the transformation medium index map into a height map for our silicon layer. The maximal effective propagation indices we can reach for the usual 500 nm and 250 nm SOI wafers are the same as in table 1. The minimal, on the other hand, are always 1.44, even for air-cladded slabs (the cut-off thicknesses for air-cladded slabs are around 105 nm for the TM mode and 25 nm for the TE). Note, however, that modes with indices close to the substrate or cladding will be very delocalized and consequently, prone to higher losses.

Patterning the height map can be done in a couple of different ways. We have develop two fabrication methods to demonstrate such GRIN media. The first uses a focused ion beam (FIB) to directly sculpt the silicon surface. The second employs high contrast grayscale electron beam lithography.

The FIB process was developed on a FEI Strata 400 using the tool feature of shape patterning. We convert the height map calculated from the slab solver into a bitmap image where the blue channel is used to control the beam dwell time (DT) at each point in the

image, allowing us to sculpt the surface of the silicon layer with high precision. This process has the advantage that once calibrated, it is consistently reproducible and precise. The DT of the ion beam is directly proportional to the value of the blue channel in the bitmap, and the milled depth in the slab is also directly proportional to the DT, turning calibration into a single constant scaling factor. Figure 6 shows an example of the level of control over the surface profile: minimal error is observed between the designed curve and the one obtained from an atomic force microscope (AFM) scan of the surface. In addition, the roughness of the silicon surface is small, reaching around 2 nm root mean square (RMS) away from the edges of the pattern (measured on the AFM).

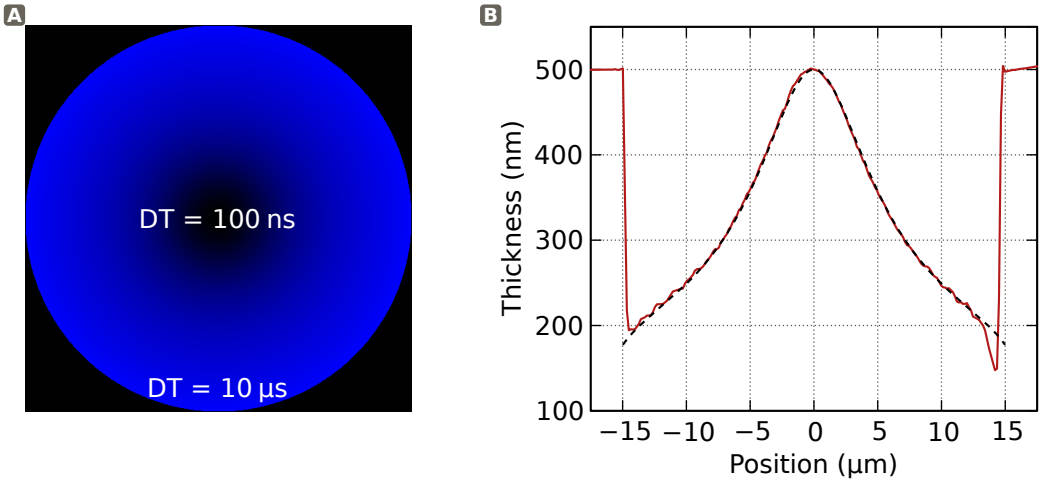

Figure 6 Direct sculpting of the silicon layer is possible using a FIB. **(a)** The designed height map (sample GRIN lens) is converted into a bitmap whose blue channel controls the DT of the ion beam from 100 ns an the center to 10 µs at the edges per beam pass. **(b)** The cross-section of an AFM scan of the silicon height (red) matches closely the design curve (black). The scans also reveals roughness around 2 nm RMS (except around the edges).

On the downside, the FIB has a few limitations. Although the surface is smooth, some scattering still occurs, which could be minimized via, for example, local oxidation

processes [62]. More fundamental is the fact that the ion milling process breaks the silicon crystalline structure and implants heavy Ga atoms in the material, inducing optical absorption. Last, and this is mostly due to the operation of this specific tool model, the only possible alignment to existing devices on the sample is through an integrated SEM, whose beam has to be manually aligned to the ion beam, resulting in errors on the order of 1 µm depending on the size of the patterned area.

This process was used in the fabrication of an integrated Luneburg lens for robust fiber-to-waveguide coupling in integrated photonics, described in detail in chapter 4.

Looking to avoid the ion-induced losses and damages to the crystalline structure, we also developed a grayscale electron beam lithography process for GRIN optical devices via dose modulation. Note that while similar processes are employed in the fabrication of diffractive optical elements, micro-electro-mechanical structures, and lower contrast gradient-index lenses [63–66], in our case the process enables strong height variations of 400 nm over less than 1 µm while maintaining control of the resist height profile on the nanometer scale with vertical resolution of approximately 10 nm.

Nevertheless, the calibration of the electron dose versus height of the developed resist is sensitive to several factors, including developing conditions, resist type, and material stack (both substrate and resist). It is also notably non-linear, as shown in figure 7 for poly(metil methacrylate) (PMMA). For these reasons, calibration curves are usually taken on the day before the device exposure by the person who will run the fabrication, since it does vary from operator to operator due to manual development of the resist.

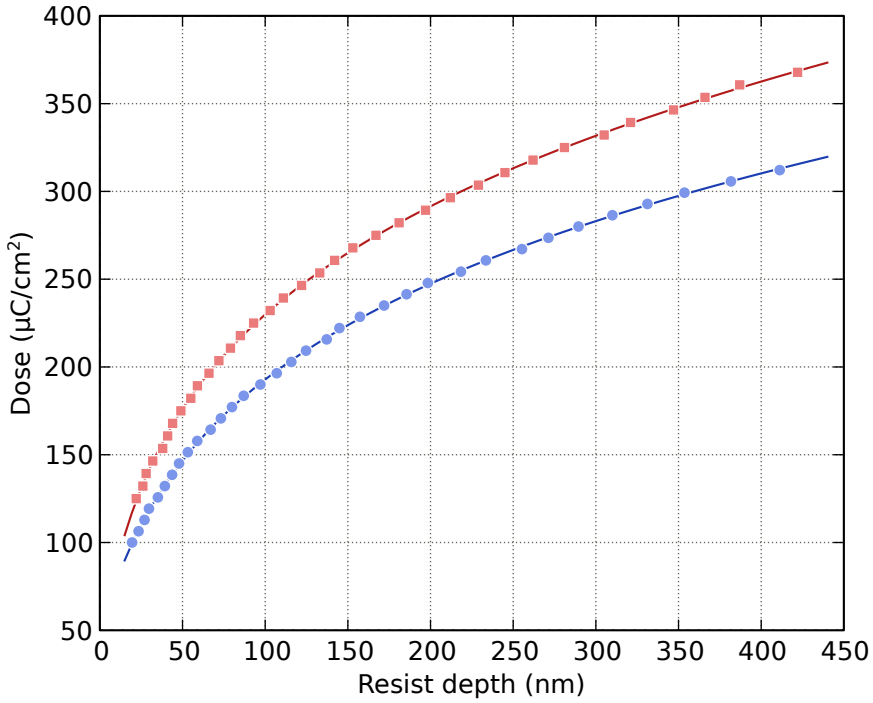

Figure 7 Example of grayscale calibration curves in PMMA taken by two different people. Strong difference is seen between the curves due to minor changes in manual development of the sample, such as exact developing time. Other factors that affect the calibration curves are general environment conditions, material stack, and resist type, as well as age.

Because the resist exposure is strongly affected by proximity effects from the point spread function (PSF) of the electron beam, the conversion between the designed height map and the electron beam dose map is done with the help of the 3-dimensional proximity effect correction (PEC) module from our design preparation tool, LayoutBeamer. To account for proximity effects in the calibration curves, the calibration pattern from which the curves are extracted is made of a number of squares with 120 µm sides, separated by around 500 µm, each exposed with a uniform electron dose. The large dimension of the squares (calculated to be around 3 times the standard deviation of our electron beam PSF) ensures that at their center they get the maximum possible exposure achieved by their respective electron

doses. The distance between the squares guarantees that they do not affect each other. After measuring the developed resit height at the center of each square, curves as the ones shown in figure 7 are obtained and used to convert the designed height map into a dose map, which is then further processed by LayoutBeamer's 3-dimensional PEC module. It is important to note that one extra calibration parameter is still required in this process, which is related to the following etch process. During etching the height profile of the resist will be transfered to the silicon layer, but depending on the etching process these materials will have different etch rates, thus a scaling factor equal to the etch selectivity must divide the silicon height map to produce the height map on the resist.

Apart from the more complex calibration, this fabrication technique also results in more surface roughness when compared to the FIB. However, this issue is not fundamental to the process, as are the issues with the ion milling. Surface roughness can be dealt with, for example, via resist reflow by heating it up above its glass transition temperature and letting surface tensions minimize the roughness. Other options are the use of oxidation techniques [62], or developing lower contrast resists and developer recipes.

The use of electron beam lithography has other advantages over the FIB. Alignment is automated on most commercial systems and typically well below 100 nm. It also allows for a much larger number of devices to be fabricated in the same amount of time, since exposing the resist typically requires much faster DT of the beam than directly milling the silicon layer.

We demonstrate this fabrication platform with a GRIN multimode waveguide bend with low mode conversion. The device and its specific fabrication are detailed in chapter 5.

2.5 Conclusions

Transformation Optics is a powerful theory for the design and analysis of GRIN devices. It allows us to freely control the flow of light throughout space via coordinate transformations. The interest in TO was greatly increased by the developments in our capability of tailoring media response far beyond the reach of natural materials. However, at optical wavelengths, the fabrication of these artificially structured materials, or metamaterials, is still challenging.

To still take advantage of TO in integrated photonics without metamaterials we developed three fabrication platforms tailored to high contrast GRIN devices with wide range of operating wavelengths. Through a few approximations we are able to avoid the need for magnetic or anisotropic materials, making the fabrication of our devices possible in a CMOS-compatible silicon platform.

Using either effective material theory or waveguide dispersion we are able to generate effective GRIN media. The fabrication methods we have developed have different strengths and weaknesses, and are better suited for different applications. The methods described here will be demonstrated in the following chapters, where we will provide additional details corresponding to the particular fabrication of each device.

3 Cloaking

Optical cloaking is, without doubt, one of the most interesting applications of TO. The prospect of invisibility has received considerable attention since its appearance [14, 16] and a great variety of designs have been proposed since [44, 67–74]. The basic idea of perfect invisibility is to open a hole in the virtual space, as shown in figure 8, and implement this hole in real space by using TO to translate the spacial deformation into material parameters. This design is in theory perfect, but the material requirements for such a device would be singular at the hole boundary [14–16]. This can be intuitively seen: light traverses the original point in virtual space instantaneously (figure 8a), and it must continue to do so after the transformation, i.e., it must also traverse the boundary of the cloaked region instantaneously, so the closer to the cloaked region, the faster the speed of light, leading to constitutive parameters closer and closer to zero (figures 8b and c). Those singular parameter values indicate that resonant metamaterials would have to be employed in the construction

of the cloak, resulting in a narrow operating frequency window [75, 76]. It has also been argued that the perfect cloak is very sensitive to imperfections [77]. Nevertheless, a demonstration of the perfect cloak was presented short after its proposal in microwaves with the help of millimeter-size metamaterial structures [45].

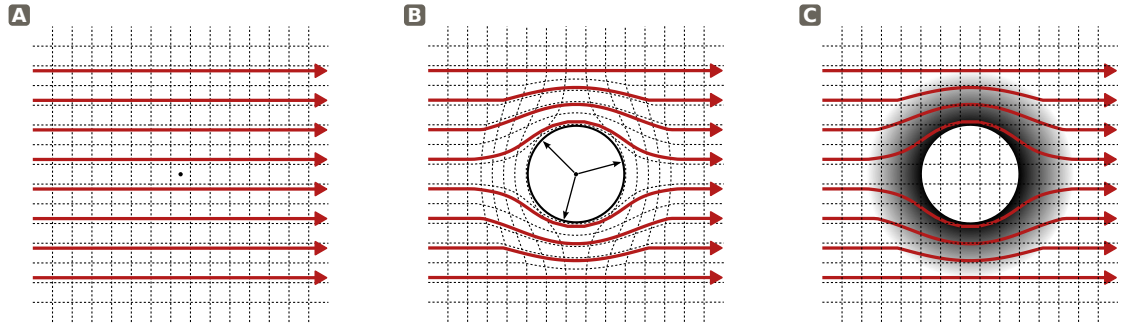

Figure 8 Perfect cloaking device. **(a)** The basic idea behind perfect invisibility is to expand a point from virtual space into **(b)** a finite area, such as a circle or cylinder. **(c)** Implementing this transformation in real space requires singular material parameters $\varepsilon_r = \mu_r = 0$ around the boundary. Because the cloaked region does not exist in the virtual space, it invisible in real space.

To overcome the fabrication issues related to singular materials and anisotropy, Li and Pendry proposed a different route to achieve invisibility by hiding a region of space under a reflective carpet [53]. Following their work, we demonstrated the cloaking effect in the optical domain at 1550 nm using sub-wavelength scale dielectric structures to form an effective GRIN medium [78, 79], as described in subsection 2.4.1. Simultaneously, similar designs were demonstrated using different fabrication methods in both optics [80] and, once again, microwaves [81].

3.1 Under the Carpet

The working principle of the carpet cloak is outlined in figure 9. When looking at a deformed mirror, the reflected image is distorted: it contains a signature of the deformation. The cloaking device is capable of reshaping the light around the mirror deformation in such a way that, regardless of the viewing angle, reflections from the mirror look perfect. Effectively, an external observer is incapable of detecting the deformation, under which objects of interest could be hidden.

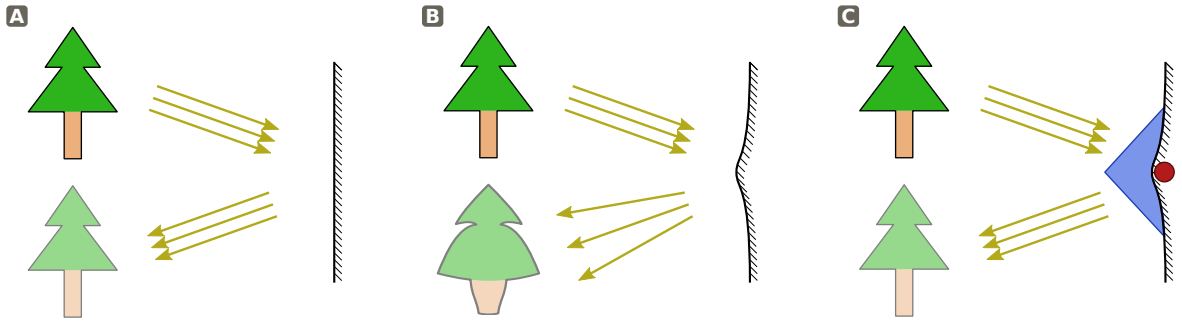

Figure 9 Carpet cloaking. **(a)** Reflections from a perfectly flat mirror have the same size and shape as the object, but when the mirror is deformed **(b)** its image will carry a signature of the deformation. **(c)** By mapping the region in front of the flat mirror to the one in front of the deformation with TO, the reflection from the latter will be indistinguishable from the reflection of the flat one, rendering the region behind the deformation concretely undetectable to an observer.

The design of this device is done via TO by deforming the region in front of the mirror together with it (figure 9b), and then mapping this deformed region to the front of a flat mirror (figure 9a). This way, the transformed region redirects the flow of light as if it were reflecting from the flat one, removing the signature of the deformation from the mirror's

reflection. The deformation and the area behind it are undetectable, and could be used as secure storage.

The presence of the reflective surface behind the cloak is necessary for the illusion. Without it, light incident in the deformed region would find an area of space not originally mapped out by the coordinate transformation—similar to, but not exactly like the hole in the case of the perfect cloak (figure 8)—breaking the validity of the transformation.

3.2 Cloak Design

One important aspect of the carpet cloak device is that it prescribes the transformation only at the boundaries of the transformation medium, leaving the interior to be freely optimized. By minimizing the Liao functional with slipping boundary conditions in the interior of the transformation [53], we are able to obtain a *quasi*-conformal mapping that can be fabricated using our effective material platform in the TM polarization, as described in subsection 2.4.1.

The range of achievable refractive indices is limited by our material selection. The limits in refractive index range and residual anisotropy will be reflected in the relative size of the deformation we are capable of hiding with respect to the size of the whole cloaking device, since the full design can be scaled up or down freely. By working with high-contrast materials our device can be made smaller for a constant size of deformation. Thus, we use silicon to form the effective core medium, since it has one of the highest refractive indices at near infrared wavelengths, enabling us to hide a deformation in the shape of a Gaussian curve with 600 nm peak and approximately 2.2 µm full width at half maximum (FWHM) in a device with 225 μm^2 area, as shown in figure 10. The resulting effective index distribution

has an anisotropy factor of 1.02 with index values ranging from 1.45 to 2.42, where the highest and lowest effective refractive index regions are located around the deformation, and the background index value of the remaining cloaking region is 1.65. The triangular shape of the device with the deformation along its hypotenuse can also be observed in figure 10.

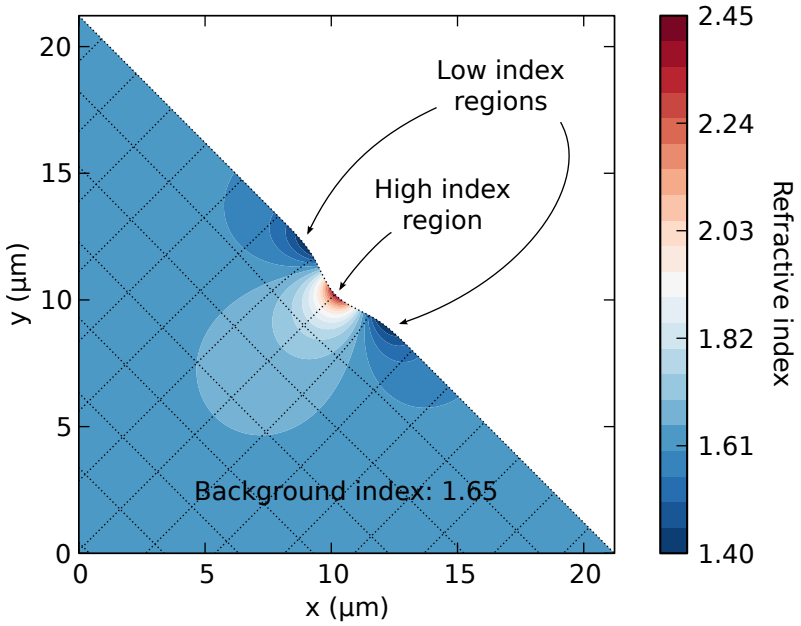

Figure 10 Refractive index distribution for the carpet cloak. We can see the highest index is in the region directly in front of the deformation, while the lowest are to its sides. The background index of 1.65 is necessary to ensure that the index range falls into the required range for fabrication in the silicon platform.

Using our effective material platform we can translate the refractive index map from the TO design (figure 10) into a volumetric fraction of silicon on the background material, SiO_2 in this case. Then we discretize the map into 50 nm square cells and apply a conventional Floyd-Steinberg dithering algorithm [59], such that the resulting "black" cells (cells where the volumetric fraction of silicon is 1) end up forming silicon pillars in the fabricated

device. The final profile of the cloak contains almost no silicon in the low index regions, whereas in the high index regions it has the largest concentration of pillars. The reflective mirror required for the device operation is implemented by a distributed Bragg reflector (DBR) also composed of Si and SiO_2. Ideally, we need a mirror that reflects all incident light at all angles of incidence, which is not valid for a DBR, so some error is expected in the reshaped reflection. Nevertheless the simulated reflectivity of our 10-period DBR is larger than 0.99 for normal incidence.

3.3 Effective Material Fabrication

The fabrication of the invisibility cloak was carried out in an SOI wafer. Dow Corning XR-1541® resist was patterned in a Jeol 9300 with a 100 kV electron beam. The pattern was transfered to the 250 nm top silicon layer using inductively coupled plasma (ICP) reactive ion etching (RIE) in Cl_2 (70 sccm) and BCl_3 (2 sccm). We then cladded the sample with approximately 2 µm of SiO_2 by plasma-enhanced chemical vapor deposition (PECVD).

An SEM image of the complete device before cladding is shown in figure 11a. We can see the effective GRIN medium of the cloak formed by the varying density of silicon pillars in figure 11b: regions of high refractive index show strong bunching of pillars, while lower index regions have only a few.

3.4 Simulation & Experiments

A silicon waveguide with dimensions 450 nm by 250 nm and tapered end was used to efficiently guide light to the device and maximize the effect of the mirror deformation. It ended

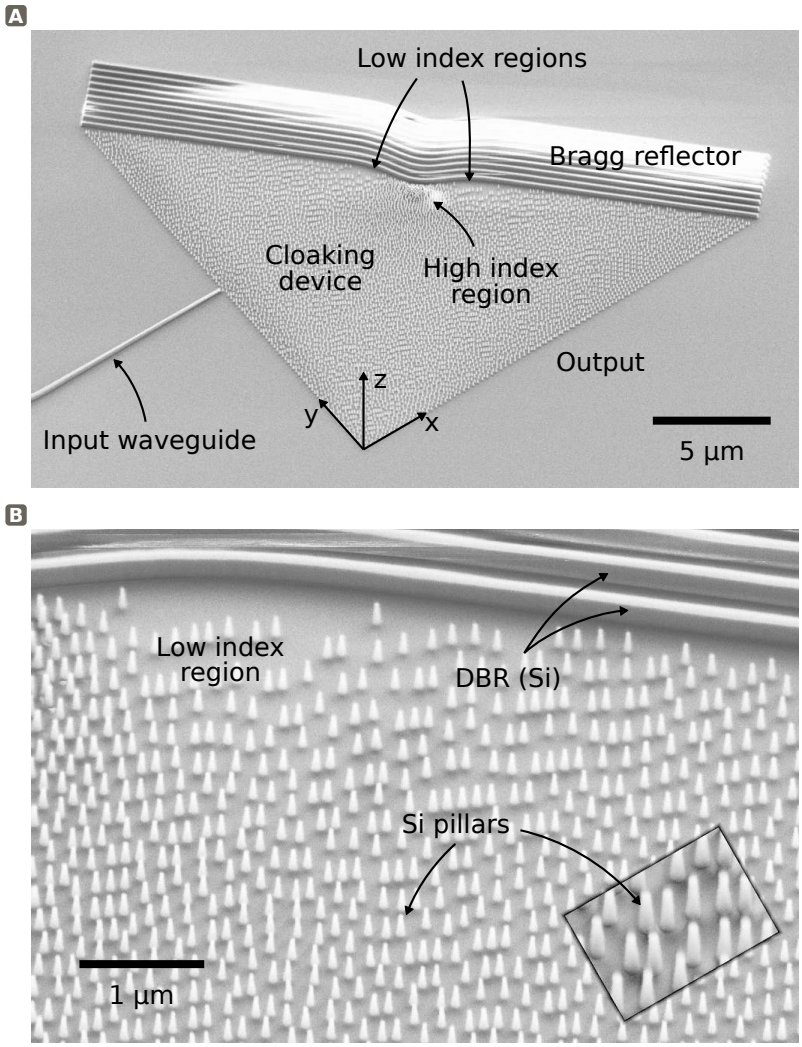

Figure 11 Fabricated cloaking device. **(a)** SEM of the whole device with the deformed DBR on the back and the input waveguide on one of the edges. The effective index corresponds to the map in figure 10. **(b)** Close up of the nanometer-size silicon pillars forming the effective material.

at the $\hat{y}$ edge of the device and pointed directly towards the Gaussian curve on the DBR, as seen in figure 11a. Note, however, that the cloaking effect occurs for light incident at any angle, not only the 45° tested here, since no constraints are introduced by the TO design, as long as the DBR reflectivity is sufficiently high.

We simulated the propagation of light in the device using the finite-difference time-domain (FDTD) method with Meep [82]. The results show that, owing to the presence of the cloak, the image of the light incident on the deformation (the region under which an object could be hidden) resembles the image of a wave propagating in a homogeneous medium without the deformation. Figure 12a shows a simulation of light propagating through a homogeneous background index of 1.65 and reflected by the DBR. Figure 12b shows the same simulation when the DBR is deformed, and figure 12c shows the simulation of light reflected by the deformed DBR but with the deformation now covered by the cloaking medium. By comparing figures 12a and b, we can see that the presence of the deformation transforms the output image of the device, measured at the output edge in $\hat{x}$. The plane reflector in a homogeneous medium distributes power uniformly along the output, whereas the deformed one results in a power gap that represents its signature. Once the cloaking medium is introduced, in figure 12c, the gap vanishes and power is again uniformly distributed on the reflected image, as in the case of the perfectly flat DBR.

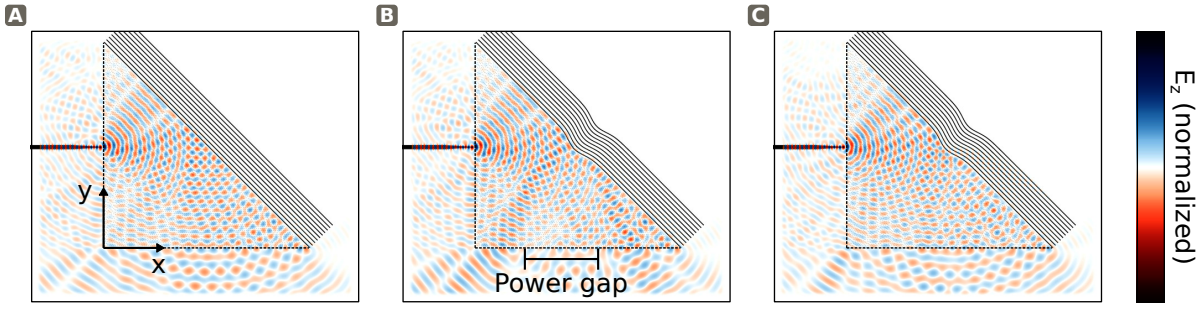

Figure 12 FDTD simulations of the cloaking device performed with the actual silicon posts designed for fabrication. **(a)** The reflection from a perfectly flat DBR results in a uniform distribution of power along the output edge of the cloak ($\hat{x}$). **(b)** The presence of the deformation changes the output by creating a power gap, the signature of the deformation. **(c)** The cloaking medium in front of the deformation reshapes the wavefronts to recover the reflection from the flat reflector.

Experimentally, we use an infrared camera to collect the reflected image at the output edge of our devices. We couple a 1550 nm laser into the input waveguide, shown in figure 11a, and capture the reflected image at the xz plane. The infrared camera was set to constant gain, brightness and contrast, and the captured images were filtered using a median filter of 15×15 pixels.

We show in figure 13 that the reflection from the cloaking device is similar to the one from a plane DBR, as in the simulations before. In figure 13b we can see the image from the plane reflector in uniform medium with index 1.65, where uniform distribution of light along the output edge is expected. In figure 13c we introduce the deformation in the DBR, resulting in an output with the signature power gap from the mirror deformation. In contrast, the output from the cloaked deformation in figure 13d shows no power gap, and the image is to the one from the flat DBR covered by homogeneous medium, as expected.

3.5 Conclusions

The results obtained in this experiment represent a demonstration of invisibility cloaking in the optical domain with only dielectric materials. By reshaping the wavefront of light according to a deformed virtual space we can effectively turn a region of real space undetectable to an external observer.

The wavelength of operation of this device is limited on the shorter side by the dispersion of silicon and size of the nano-pillars (such that the effective material regime is valid). On the longer wavelengths the reflectivity of the DBR sets the limit of operation. According to our simulations, this bandwidth is approximately 400 nm around 1550 nm due

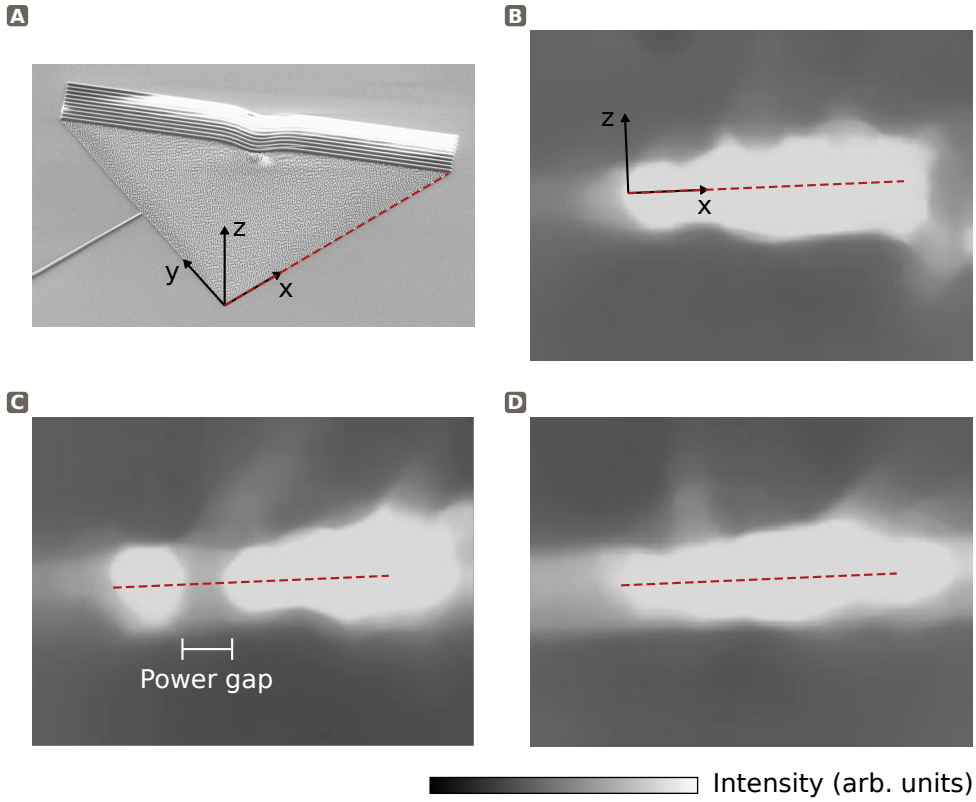

Figure 13 Experimental demonstration of the cloaking effect. **(a)** The results shown are images from the output edge of the device (red) captured by an infrared camera. **(b)** Image from the reflection of a flat DBR in with homogeneous medium. **(c)** Reflection from a deformed DBR in homogeneous medium showing the expected power gap, the signature of the deformation. **(d)** Reflection from the same deformed DBR as before, but now covered by the cloaking medium. The power gap vanishes and the output becomes similar to the one of the flat DBR, as expected. These results correspond to the simulations in figures 12a, b and c respectively.

to the high index contrast between Si and SiO_2.

The demonstrated cloak could, in principle, be reproduced in much larger dimensions using fabrication techniques such as deep ultra-violet (DUV) photo-lithography or nano-imprint. This device has direct applications in defense, such as camouflage and optical illusions, and communications, such as correcting defects in satellite mirrors, among others.

The freedom of tailoring the trajectory of light by TO and the capability of implementing these designs in the optical domain without the need of material resonances opens up many other possibilities, specially where wide operation bandwidth is desired. For example, the same fabrication platform developed here has been used to demonstrate a wavelength-independent light concentrator aimed at solar energy applications [83, 84].

4 Luneburg Lens

Among GRIN structures, lens-like media were one of the first focuses of interest from the scientific community [1–5, 7, 8, 12]. GRIN lenses have the potential to successfully solve aberration and dispersion problems inherent to conventional homogeneous lenses. In special, the Luneburg lens [12] is an aberration-free and comma-free spherical lens with a refractive index profile appropriate for dielectric-only implementation.

The advantage of fabricating the lens with dielectrics is the same as for other GRIN devices, including the ones designed via TO, such as the cloak in the previous chapter: the range of operating wavelengths is limited only by material dispersion (and, of course, specific design characteristics), which is usually low in their transparency window, specially when compared to resonant metamaterial implementations. In contrast, resonant metamaterials are capable of a much wider range of effective parameters, allowing for negative refraction and perfect lenses [39–42], for example.

Using the silicon platform and direct patterning using a FIB we fabricated and demonstrated a dielectric-only Luneburg lens for integrated photonics [85, 86]. Although a demonstration of the standalone lens in silicon was presented during the realization of this work [63], here we integrate the lens with current silicon photonic devices and use it to improve the coupling sensitivity between channel waveguides and single-mode optical fibers, a key feature for the packaging and yield of nanophotonic chips in future optical communication interconnects. In the following sections we will discuss the properties of the Luneburg lens that make it attractive for robust fiber-to-waveguide links, its design and implementation in silicon, and the experimental results obtained for the coupling sensitivity.

4.1 Optical Properties

The Luneburg lens is an aberration-free and comma-free spherical GRIN lens with focal spot located on the its circumference [12, 25]. In a conventional refractive lens, the focal point changes depending on the distance of the incoming ray to the optical axis due to aberrations, so that rays coming parallel to the axis will not all focus at the same spot, as illustrated by figure 14a. In the Luneburg, the focal spot is independent of the distance to the optical axis (figure 14b), i.e., beams coming with same $\vec{k}$ direction will be focused on the same spot regardless of their incident position on the lens.

Another characteristic of the Luneburg lens is, of course, its index profile, given by the equation:

$$n(\rho) = n_0\sqrt{2-\rho^2} \tag{4.1}$$

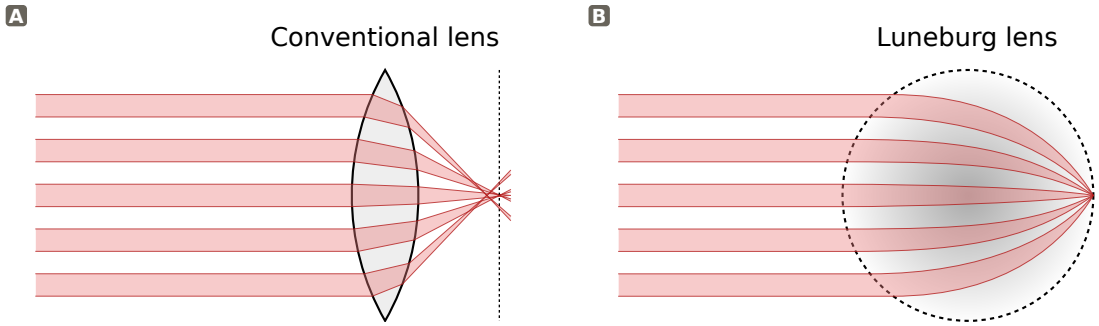

Figure 14 Comparison between a conventional and a Luneburg lenses. **(a)** Aberrations in a conventional lens cause its focal plane to change depending on the distange of the incoming beam to the optical axis. **(b)** The Luneburg lens is aberration-free, thus all incoming light with a fixed $\vec{k}$ will focus on the same diffraction-limited spot. The lens itself is spherical with refractive index varying as a function of the radial position and possibly matched to the surroundings at the edge, making it also free of reflections. The loci of its focal points is not a plane, but the circumference around the lens itself.

where $\rho \in [0, 1]$ is the normalized radial position inside the lens, and n_0 is a constant. The rotationally-symmetric index profile can be freely scaled by n_0. This degree of freedom allows us to match the edges of the lens at $\rho = 1$ to the surroundings index and eliminate reflections at the lens boundary. This is once again in contrast to a conventional lens, where the use of anti-reflective coatings is necessary to avoid reflections. It is important to note that while a conventional lens operates through refraction at material boundaries, the Luneburg—and GRIN device in general—control the flow of light through the gradient of the refractive index, possibly avoiding reflection, diffraction, and other scattering phenomena that usually impact in the loss or transparency of the system.

The lack of sensitivity of the Luneburg lens focus to the exact position of the incoming light has direct application in the robust coupling of systems at different length scales. In special, coupling between optical fibers and integrated waveguides are fundamental for integrated optical communications. Low-loss coupling can be achieved by adiabatically con-

verting the modes between the two structures with inverse nanotapers [87–90], but to achieve high efficiency they require stringent alignment control, which is a problem for future mass production and commercialization of those systems. Therefore, there is a need for a coupling device with improved robustness to misalignments: a device that is able to reliably collect light coming to the chip and deliver it to the system's waveguides. By adding the Luneburg lens to the taper design we benefit from its fixed focal spot position and significantly decrease the alignment sensitivity of the bare inverse taper to optical fiber.

4.2 Thin Film Design

The refractive index of the Luneburg lens was implemented in a GRIN medium fabricated by controlling the thickness of the guiding layer in our SOI wafer, as detailed in subsection 2.4.2. We designed the slab to have a Si core and SiO_2 substrate and cladding, and to operate in the TE mode. Using an inverse slab solver, i.e., solving the thickness of the dielectric slab for a required guided wavenumber, we translate the index in 4.1 to a height profile for the lens as a function of its radial coordinate ρ, shown in figure 15. The constant n_0 was used to match the refractive index of the surrounding, minimizing reflections. We can see that the 41% contrast in refractive index of the lens results in a slab core ranging from 0 to 82 nm in thickness.

So far we kept the in-plane size of the lens (radial coordinate) normalized, since it can be freely scaled without changes in the index profile or slab height map. We choose the final device size based on two other competing factors: (a) a larger lens results in smaller alignment sensitivity in the coupler, since the fiber and waveguide can be further misaligned while the

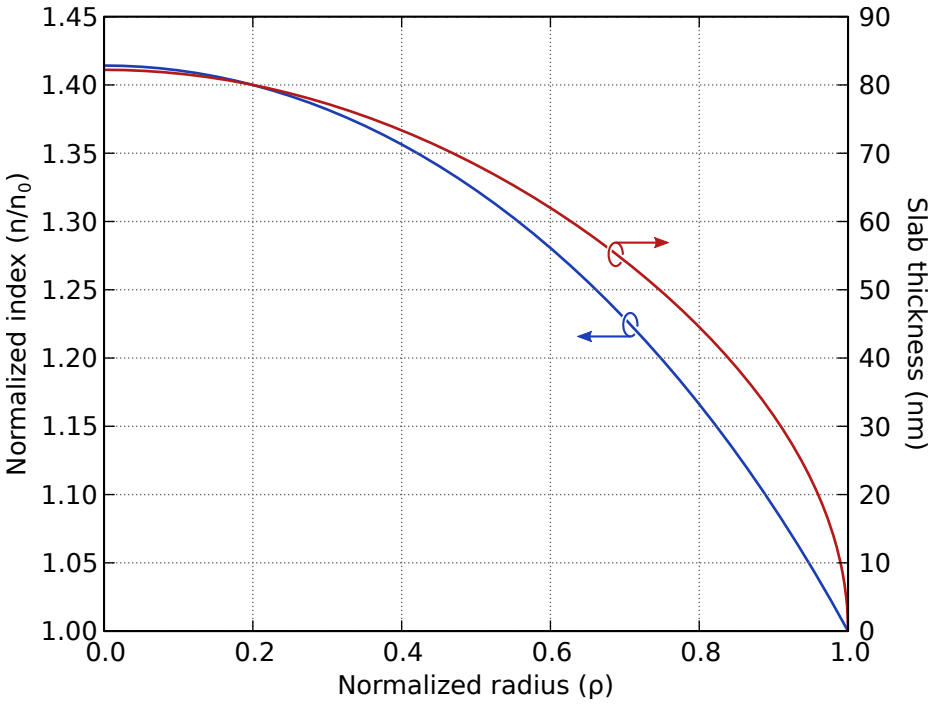

Figure 15 Normalized index profile for the Luneburg lens (blue), given by (4.1), and corresponding silicon slab thickness (red) to generate it. We assume the Si slab surrounded by SiO_2 and $n_0 = n_{SiO_2}$

lens is still collecting light from the fiber; (b) because the fabrication is not perfect, the lens will introduce losses to the system, which will be higher the longer light has to propagate through the lens medium. We found a good compromise between these factors to be a lens with 30 µm in diameter, which, as we will see, clearly shows the improvement in robustness without introducing excessive amounts of loss.

4.3 Direct Silicon Patterning

Patterning of the height profile in the 250 nm silicon layer of the SOI wafer was done by FIB. This process of direct sculpting the silicon surface is accurate and precise. The ion beam is controlled directly by the pattern via a bitmap file as described in subsection 2.4.2. After

patterning the lens, we scanned it in an AFM and compared the surface profile to our original heigh map design. The result, displayed in figure 16, shows the great agreement between the two and the small surface roughness left on the silicon layer.

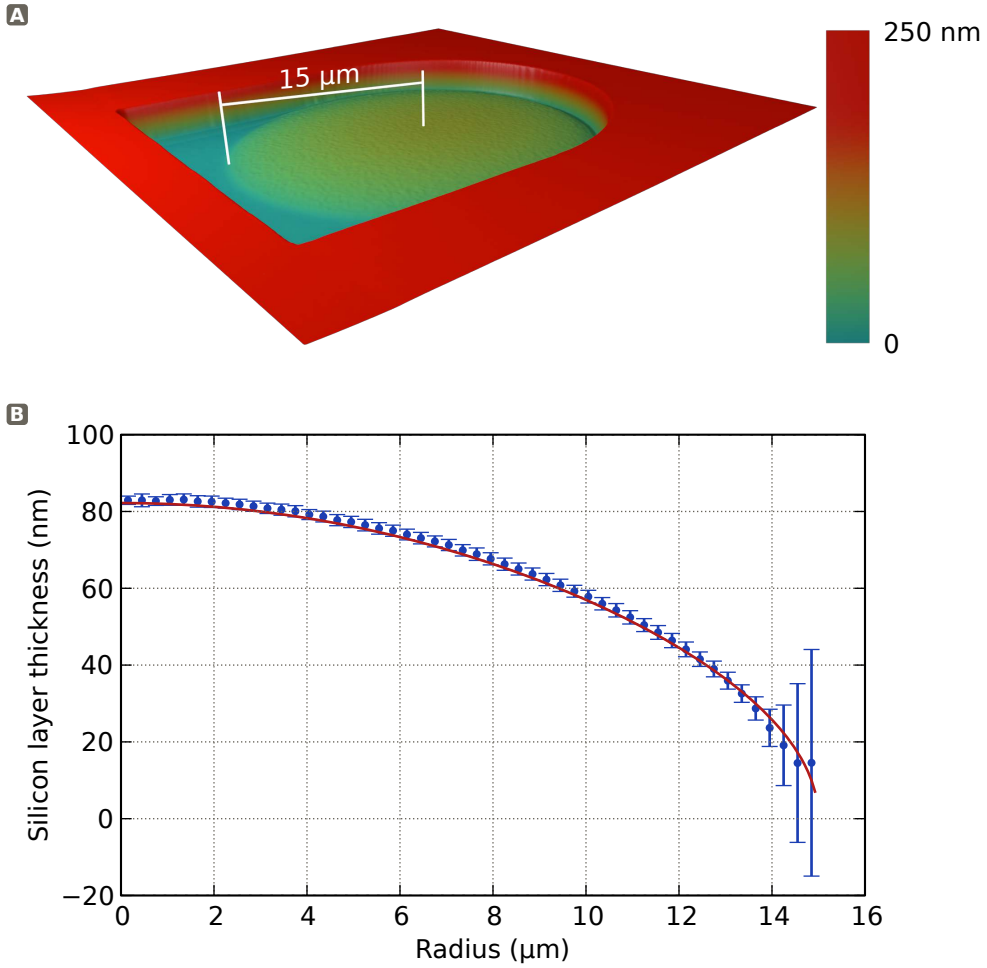

Figure 16 AFM image from the Luneburg lens. **(a)** Complete scan of the device, showing the small surface roughness left by the FIB. **(b)** Comparison of the patterned height profile (blue dots) and the design (red line) curve, showing great agreement. The height error significant only at the very edge of the lens.

To achieve this patterning control it was vital to eliminate beam drifting due to substrate charging during the milling process. In order to do so, we dipped the samples for

approximately 10 s in buffered oxide etch (BOE) 6:1 immediately before placing them under vacuum to eliminate the native SiO_2 that forms on the Si surface of the SOI wafer. We also mounted the samples in the metallic holder of the FIB tool using a conductive double-sided tape which had its tip folded over on the top surface of the sample (towards the edges,away from the devices) to decrease the top silicon charging.

The silicon channel waveguides and inverse tapers were fabricated in the same sample before the Luneburg lens. They were defined by electron beam lithography on PMMA and transfered to the silicon layer by ICP RIE. Then the lens was patterned with the help of alignment marks made during the fabrication of the waveguides. The whole sample was afterwards cladded with approximately 2 µm of SiO_2 by PECVD . Finally the sample was diced and its facets polished to reduce scattering in the coupling region due to the roughness of the dicing saw.

4.4 Robust Coupling

We measured the sensitivity of the Luneburg coupler and compared it to an inverse taper fabricated on the same chip. We show that even with the optical fiber misaligned to the taper, the Luneburg mediated coupler will focus light onto the taper tip, minimizing the sensitivity to the misalignment, as illustrated in figure 17. The taper is 75 µm long with width linearly varying from 120 nm to 450 nm, matching the waveguide. The experiments were performed by coupling light at 1550 nm from a single mode lensed fiber with spot size around 3 µm onto the Luneburg coupler and, as reference, to an inverse taper coupler without the Luneburg lens. The spot size that the Luneburg lens creates depends on the k-vector distribution of

the input light on the lens itself, so we still use an inverse taper after the Luneburg for efficient mode conversion. The taper also helps with the index matching between the edge of the lens and the silicon waveguide. The input fiber was mounted on a piezoelectric stage, such that by moving it and monitoring the transmitted power we can generate a map of the misalignment loss versus alignment error. The output signal was collected by a 10× objective, filtered by a TE polarization filter, and measured on a photo-detector.

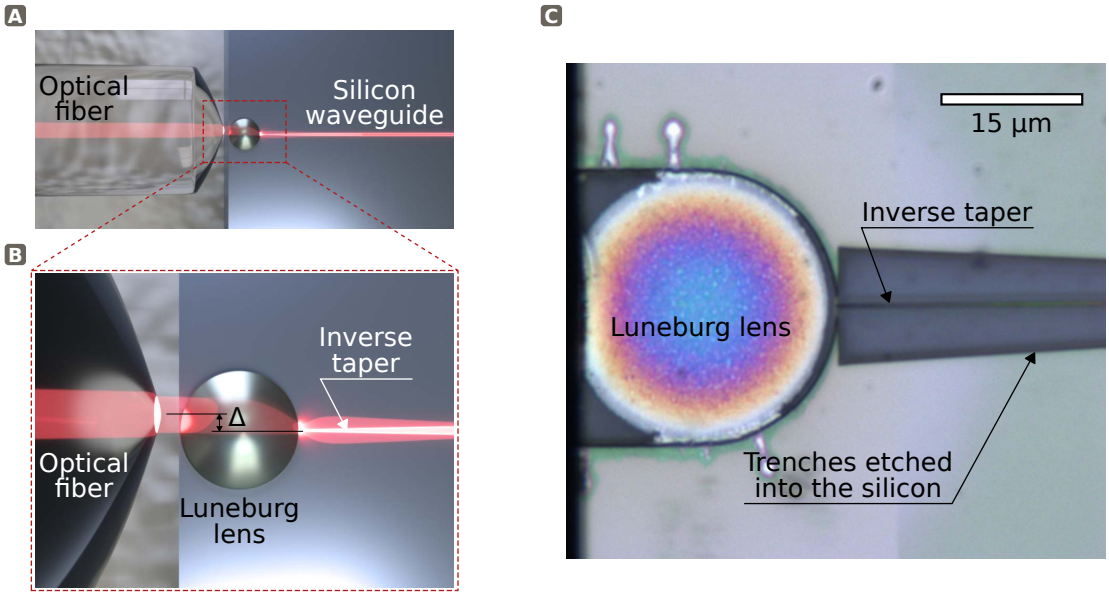

Figure 17 Luneburg-mediated coupler. **(a)** Light from the optical fiber is coupled to the inverse taper through a Luneburg lens. **(b)** Because the lens is aberration-free, it focuses the laser at the inverse taper even if the fiber is misaligned to the optical axis, decreasing the sensitivity of the system to this misalignment. **(c)** Optical microscope image of the fabricated device and inverse taper. The colors in the lens are an interference pattern formed by visible light, an evidence of its height profile.

The transmission map thus generated, displayed in figure 18, shows robust fiber-to-chip coupling with decreased alignment sensitivity by the Luneburg coupler. We plot the maps from 2 Luneburg couplers and 2 inverse tapers-only couplers obtained by moving the input optical fiber along the sample edge (horizontal direction) and perpendicular to the sample

plane (vertical direction). On the cross-section plots of figure 18b we see that the Luneburg coupler results in about 6 dB gain over the inverse taper at 4 µm misalignment in the horizontal direction. At the same time, we see that on the vertical direction, which is not accounted for by the planar lens design, the presence of the lens does not affect the sensitivity.

Note that the plots in figure 18 are normalised by the maximal transmission of each device, excluding thus their insertion loss, which is around 6 dB larger for the Luneburg coupler than for the inverse taper-only coupler. This loss is not fundamental to the design, but a result of the FIB process, due to the damages to the crtstalline structure of the silicon layer, heavy ion implantation, and residual surface roughness, which can all be improved by further developments in GRIN media fabrication.

The continuous curves in the plot are simulated results obtained from full 3-d simulations performed with Comsol Multiphysics®. The fiber in the simulations was replaced by a Gaussian source with standard deviation 3 µm at 1 µm distance from the sample edge. The simulation domain included both the Luneburg lens and the inverse taper in their real size. These results indicate no additional insertion loss from the Luneburg lens, confirming our conclusions that the losses are due to fabrication imperfections.

4.5 Conclusions

We demonstrated a GRIN Luneburg lens coupler with reduced misalignment sensitivity for robust fiber-to-chip optical links. This work is a first step in the direction of integrating complex media with conventional photonics to improve the characteristics of the latter by leveraging the key strengths of GRIN devices.

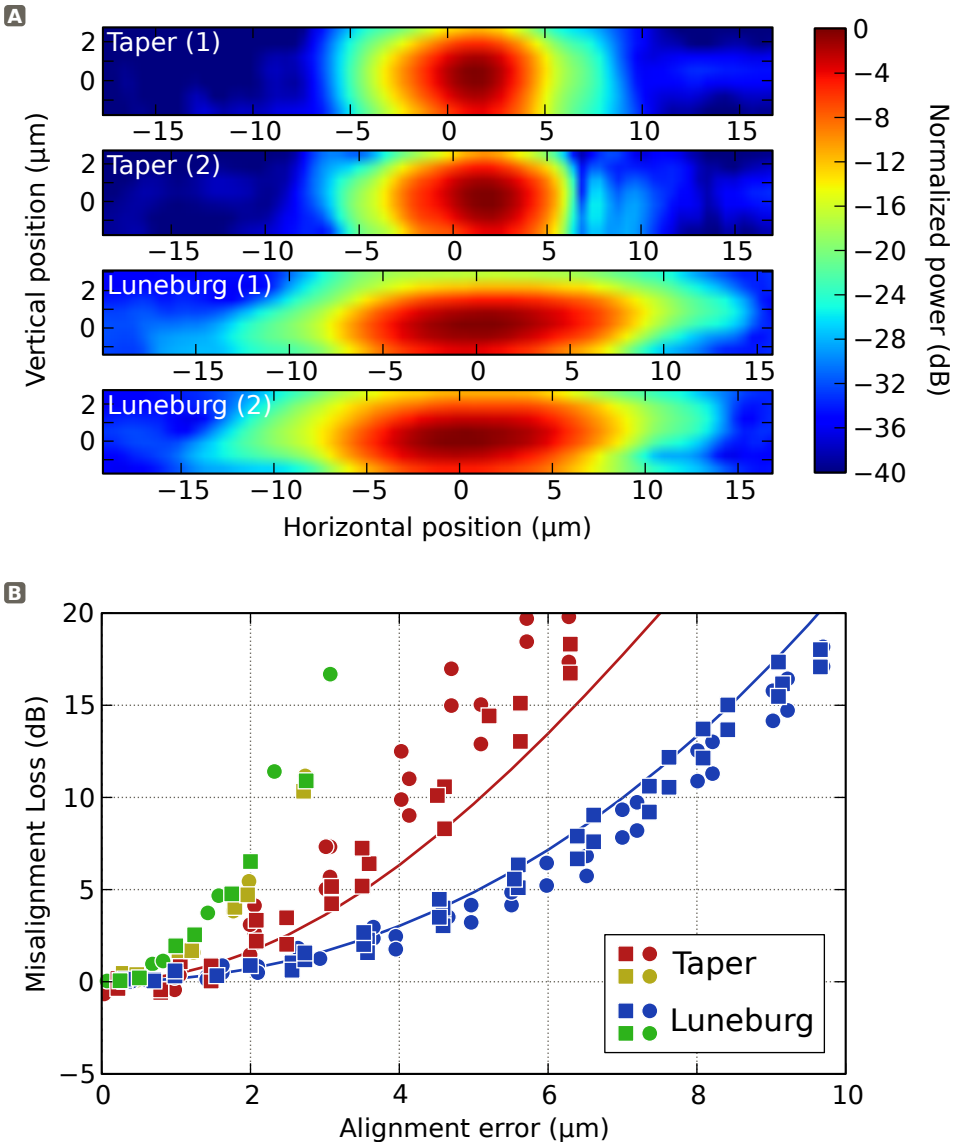

Figure 18 Coupling sensitivity measurements. **(a)** Normalized transmission maps of the taper-only and Luneburg-mediated couplers as the optical fiber is moved along the chip edge (horizontal) and perpendicular to the chip (vertical). Two samples of each type were measured. **(b)** Misalignment loss extracted from the transmission maps by taking their cross-sections through the point of maximal transmission in the horizontal (red and blue) and vertical (yellow and green) directions. The points in the horizontal direction show that the loss introduced in the Luneburg couplers grows much slower with misalignment than in the taper-only couplers. Both types of couplers behave similarly with respect to vertical misalignment. The continuous lines are simulations using the designed geometries—no fitting parameter was used—and match well the corresponding experiments.

The fabrication process of this device, based on direct patterning of the silicon layer by FIB, is promising due to its precision and accuracy, even though losses are introduced. Our ability to fabricate integrated compact GRIN structures brings a new class of devices to improve existing nanophotonics technology, such as the Luneburg coupler here demonstrated, or to enable new functionalities for light propagation.

5 Multimode Photonics

Multimode fibers are widely used in the field of optical communications for short and medium range transmissions. In integrated photonics, on the other hand, the absolute majority of research is conducted in single-mode waveguides, to avoid the problems of inter-mode coupling, which would limit data rates [91] and negatively affect the system by introducing loss or dispersion. However, multimode waveguides also present important benefits, such as easier coupling to optical fibers due to higher numerical aperture, and lower propagation losses due to less field interaction with the waveguide sidewalls. They could also enable modal multiplexing of communication channels in the same way as wavelength multiplexing is currently used, increasing the bandwidth of each link by folds, as long as the channels have minimal crosstalk.

Inter-modal crosstalk does not occur in fields propagating in a perfectly straight multimode waveguide. They are induced by bends or other perturbations to the waveguide

geometry because of the modal mismatch between the straight and the curved sections. Figure 19 shows the mode mixing in a 78.8 µm radius bend on a 4 µm wide silicon waveguide, which supports 16 modes at 1550 nm wavelength. It shows the inter-mode coupling caused by exciting each of the first three modes of the straight waveguide at the bend input. We can see that a superposition of many modes is obtained in the output of the bend in all three cases; for excitation of the fundamental mode only, for example, the output contains 71% of the excited power converted into the second order mode, and 23% into the third (figure 19a). Such strong crosstalk would severely limit data rates in a communication link. The simulations were performed for the magnetic field perpendicular to the propagation plane (TM mode) using the FEniCS solver [92].

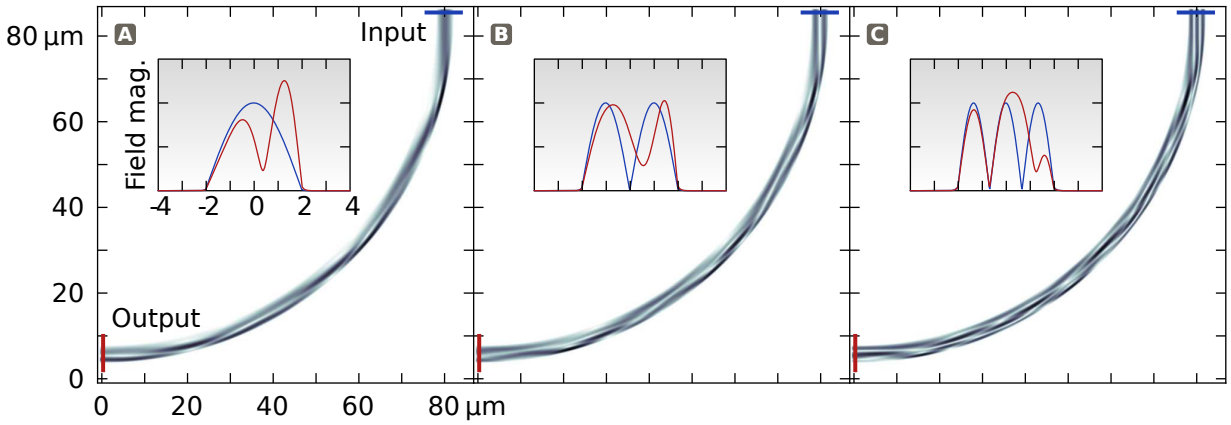

Figure 19 Simulations of a circular multimode bend. The squared magnetic field magnitude ($|H|^2$) is plotted. Only the first, second, and third order modes of the input waveguide is excited in **(a)**, **(b)**, and **(c)**, respectively. The input fields excite many higher order modes in the bend, as evidenced by the inset cross-section plots of the input (blue) and output (red) of the bends. The width of the waveguide is 4 µm and the bend radius is 78.8 µm.

One possible solution to bending multimode waveguides without inter-modal mixing would be to employ much larger radii, but those would be prohibitive to nanophotonics

integration due to their large size. For example, in the 4 µm wide waveguide considered earlier, a bending radius of more than 1 mm is necessary to ensure that 95% of the optical power remains in the fundamental mode throughout the bend.

Our work combines a large-scale inverse design approach based on TO with unique high-contrast grayscale lithography to demonstrate the possibility of integrated multimode photonics with minimal mode coupling [93]. We show an exemplary device, a multimode bend such as the one in figure 19, where the transmission of the fundamental mode is comparable to the transmission of a single mode waveguide.

5.1 Transformation Optics for Multimode

The TO design of a 90° multimode bend is based on bending a virtual space where the multimode waveguide is perfectly straight. Because light propagates identically in both real an virtual space, the multimode bend thus designed does not introduce inter-mode coupling, just as the straight waveguide in virtual space. Additionally, due to this same principle, the phase relationship between the modes is also preserved throughout the bend, which is an important factor for other phase-sensitive applications, such as non-linear phase matching or resonant cavities.

Special attention must be given to the interfaces between the TO bend and the straight waveguide. If this interface is not matched, each mode in the straight section will excite many modes in the bend, similarly to the circular bend presented in figure 19, immediately producing inter-modal mixing, even if the propagation along the bend does not. Therefore the bend transformation must smoothly transition from the same shape as the waveguide at

its end facets to the curved space.

To design this transformation we developed a general TO optimization method for multimode devices with minimal inter-mode crosstalk while accounting for the limited range of refractive indices and anisotropy. The structure is optimized over a large space of smooth transformations parametrized by general Fourier and Chebyshev series coeficients to find the minimal worst-point anisotropy that satisfies the refractive index constraints. The transformations are parametrized in such a way that they match the multimode waveguide profile at the end facets by construction. This method is in contrast to the *quasi*-conformal map optimization used in chapter 3 for the cloaking device, where only the average anisotropy is minimized, the index contrast is not directly incorporated as a constraint, and the complete boundary of the transformation must be specified *a priori*.

The optimized bend profile has an effective radius of 19.7 times the waveguide width (similar to the cloaking device and the Luneburg lens in previous chapters, the bend geometry can be freely scaled). Using the same 4 µm wide waveguide as before, the resulting effective radius is 78.8 µm. We simulated this bend to compare it to the circular bend presented in figure 19. The difference in mode mixing from the TO design is clearly represented by figure 20, where the same first three waveguide modes are excited at the input facet, but this time propagate with minimal mixing to higher order modes.

The actual refractive index profile of the bend is shown in figure 21a. In the cross-section plots we clearly see the general characteristic of the profile: the index decreases from the inside to the outside of the curve, as would be intuitively expected from a cylindrical transformation. The refractive index contrast of the GRIN medium is larger than 2, but still

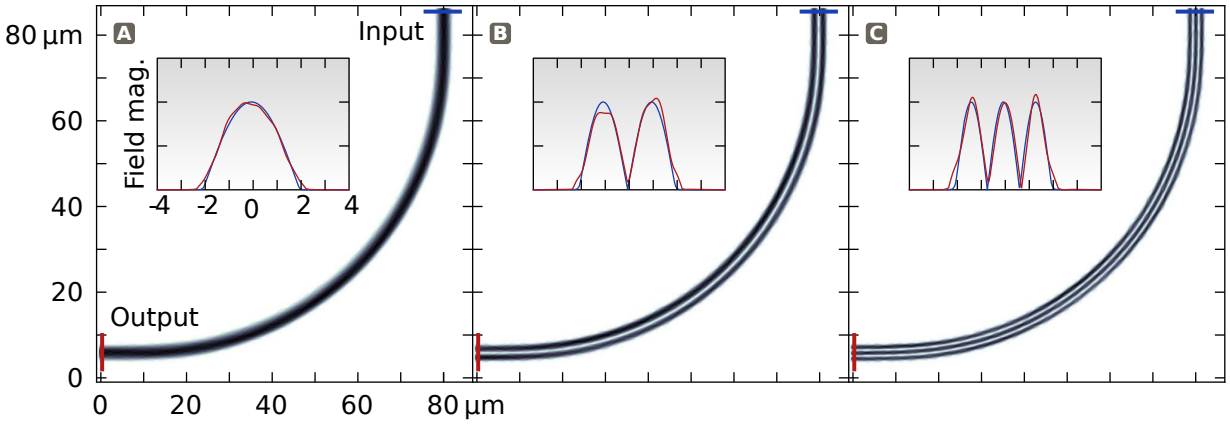

Figure 20 Simulations of the optimized multimode bend. Same as in figure 19, but using the GRIN medium optimized and designed via TO. In this case, the three modes are preserved throughout the bend, indicating minimal inter-mode coupling.

constrained by the achievable range in the silicon material platform.

5.2 Bend Fabrication

Because of the long propagation length in the GRIN medium, we need a fabrication process that reduces losses to a minimum. Both methods developed earlier for GRIN fabrication resulted in somewhat lossy media due to scattering in the case of discrete structures, and absorption in the damaged silicon crystal for the FIB method. To fabricate the multimode bend we developed a third alternative in GRIN fabrication. As before, we use the thickness of the silicon slab to control the in-plane effective index of the structure, but instead of directly milling the height map, we used electron beam grayscale lithography. Similar processes are used in the fabrication of diffractive optical elements, micro-electro-mechanical devices, and lower index contrast lenses [63–66] with less than 100 nm height variations over distances of tens of micrometers. Our process, on the other hand, enables strong height variations of 400 nm over less than 1 µm, as required by the multimode bend profile shown in figure 21b,

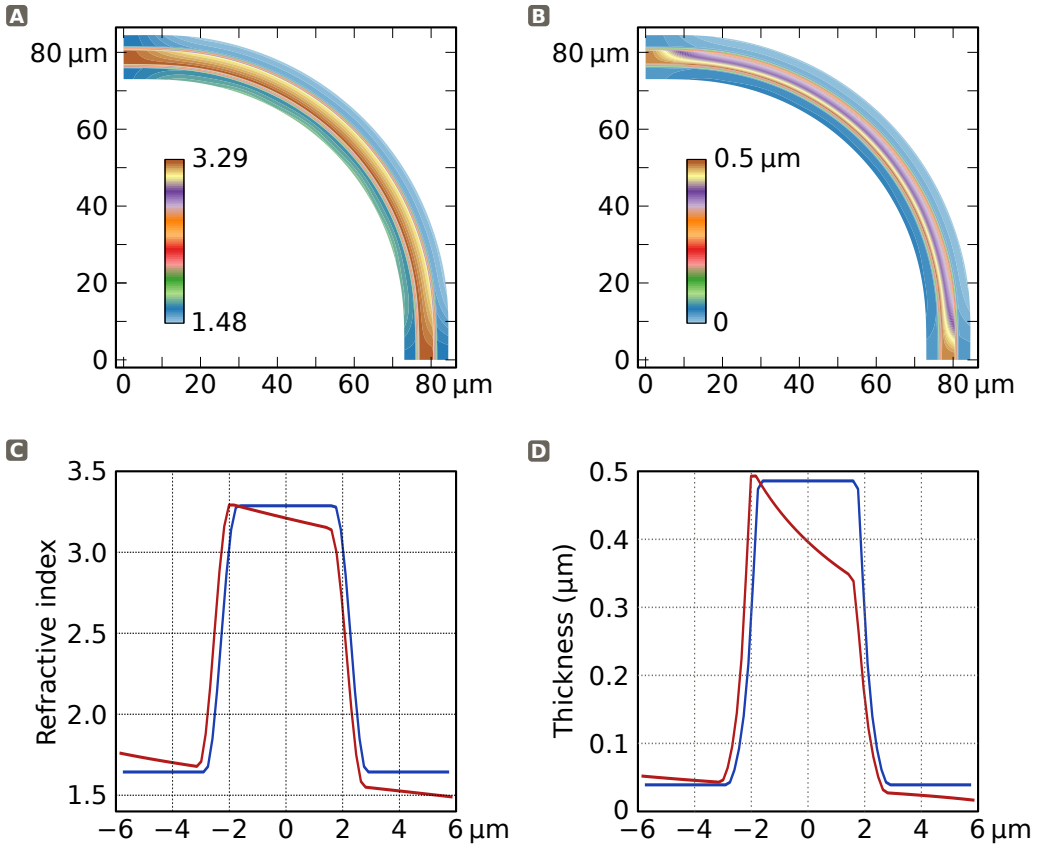

Figure 21 Optimized multimode bend. **(a)** Graded refractive index map of the multimode bend. The index ranges almost all the way from the index of SiO_2 to the effective index of a 500 nm Si slab in SiO_2. **(b)** Height map of the silicon layer corresponding the optimized index map. **(c)** Cross section of the refractive index at the input facet (blue) and at the center of the bend (red). The small index variation is responsible for the curvature of virtual space. **(d)** Cross-section of the height map of the silicon layer at the input facet (blue) and center of the bend (red). The facet geometry must match the geometry of the straight waveguide connected to the bend, which means that the straight multimode waveguide must have a thin slab of silicon on its sides. At the center, the variation in height required to generate the small index variation in the core of the waveguide bend is much more pronounced than on its sides, which requires high contrast and high resolution grayscale lithography

with resolution of approximately 10 nm.

We use an SOI wafer with 3 µm thick buried SiO_2 and 500 nm of Si on top. The grayscale profile is first created on a 430 nm layer of PMMA with spun on top of the Si using

dose modulation on a 100 kV electron beam tool. Careful calibration is required for this process, as described in subsection 2.4.2. The used doses varied from 125 µC/cm^2 up to about 350 µC/cm^2. The resist was developed in a mixture of isopropyl alcohol (IPA) and deionized water in proportion 2:1 for 1 min, followed by 30 s of IPA rinse. To reduce the roughness on the resist, a 1 min reflow at 145 °C followed. The height profile thus obtained was transfered to the silicon layer via ICP RIE in SF_6 and C_4F_8 chemistry. The etch selectivity of Si with respect to PMMA is very close to 2:1, so the height map in figure 21b is divided by 2 to be patterned in the resist. Moreover, very low electron doses on the resist tend to result in rougher surfaces than higher doses (and also require a large shot pitch in the electron beam tool), so we define the minimal developed depth on the resist to be 50 nm. Thus, the depth of the developed resist d_{PMMA} will be given by:

$$d_{\mathrm{PMMA}}(x,y) = d_0 + \frac{d_{\mathrm{Si}}(x,y)}{s} = d_0 + \frac{t_{\mathrm{Si}} - h_{\mathrm{Si}}(x,y)}{s} \tag{5.1}$$

with d_{Si} the etch depth on the silicon slab, $d_0 = 50$ nm and the etching selectivity $s = 2$. Naturally, the etch depth of the silicon layer is given by the difference between the layer thickness in the SOI $t_{\mathrm{Si}} = 500$ nm and the desired height map h_{Si} from figure 21b. Note that (5.1) assumes constant etching selectivity throughout the whole process. In our case, the etching tool uses a lighting step of about 8 s with different selectivity before the actual process is established. This step is acceptable at the beginning of the process if it only etches the PMMA, i.e., the regions with least resist are thick enough to last the complete lighting step without exposing the silicon layer. Once the silicon is exposed, the selectivity must remain constant, hence we cannot stop and restart the process—the required thickness must

be etched in a single run—so careful calibration of the etch time is required. The resulting GRIN medium is shown in figure 22. We can see from the SEM images that the surface seems very smooth.

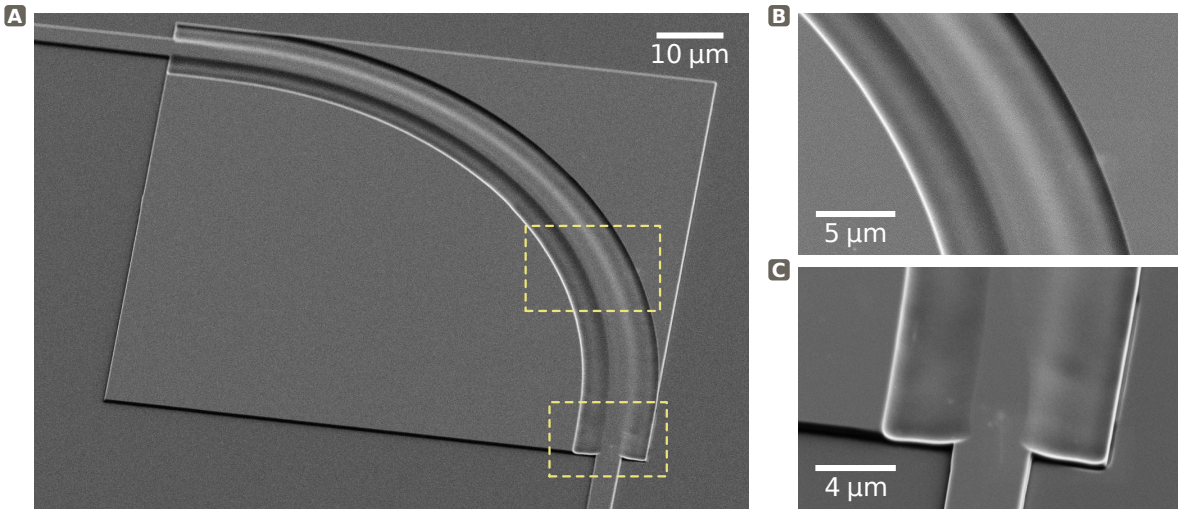

Figure 22 SEM image of the fabricated multimode bend. **(a)** The silicon layer is patterned with the desired height map by grayscale lithography on PMMA and etching. **(b)** Close up of the bend showing the smoothness of the etched surface. **(c)** Connection between the end facet of the GRIN bend and the straight multimode waveguide. This connection must be matched to avoid mode mixing.

After the GRIN medium fabrication, we patterned the remaining waveguides using conventional electron beam lithography process. One last lithography step was used to define input and output focusing grating couplers [94–97] with period of 520 nm and etched depth of 140 nm. The complete system can be seen in figure 23.

5.3 Modal Crosstalk Measurement

Measurement of the mode mixing was performed on the fundamental mode of the 4 µm wide waveguide (same as in the simulations in figures 19 and 20). Light at 1550 nm was coupled

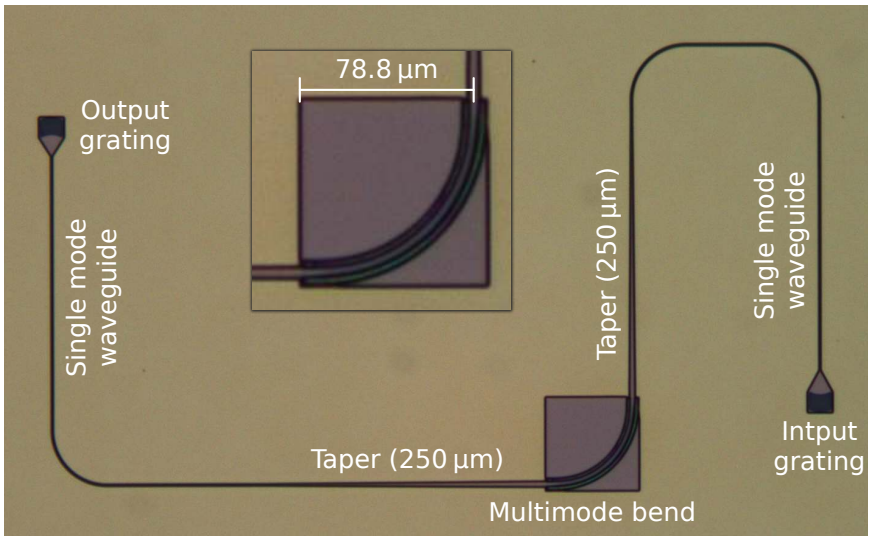

Figure 23 Optical microscope image of the complete multimode testing link. The input and output gratings are connected to single mode waveguides, which in turn are connected to the multimode bend through long tapers, such that only the fundamental mode is excited at the bend input and, likewise, only the fraction of power in the fundamental mode at the output is transmitted by the taper. Any higher order modes excited along the bend are radiated and converted into transmission loss in the link.

into single mode waveguides via a grating coupler. The waveguide is adiabatically expanded to a width of 4 µm, so that only its the fundamental mode is excited, and then connects to the optimized multimode bend. After the bend another adiabatic taper connects it to a single mode waveguide that is coupled out of the sample by an output grating (see figure 23) and then detected by a power meter.

Because of the long taper after the bend, only the fundamental mode of the multimode waveguide is coupled to the single mode one. This way, any higher order modes that are excited in the bend due to inter-modal mixing will be radiated away, and the transmitted power by the system will be proportional to the transmission of the fundamental mode through the multimode bend plus the base insertion loss. We compared the transmission of

our optimized bend to a circular multimode bend and to a conventional single mode bend (without tapers) as base insertion loss reference. The results, displayed in table 2, show that the optimized bend not only outperforms the circular multimode bend, as expected from the simulations, but also has similar performance to a single mode bend for the transmission of the fundamental mode, indicating minimal mode mixing. We also believe that the losses inevitably introduced by the grayscale fabrication are compensated by the naturally lower losses of multimode waveguide, giving the optimized multimode system the same total insertion loss as the single mode one. The difference in transmission between the two multimode bends, approximately 14.5 dB, agrees very well with the simulations in figures 19 and 20, which show a difference of 13.6 dB. The distribution of measurements collected from the multimode samples are also displayed in figure 24.

Table 2 Transmission measurements for each type of fabricated bend when excited with the fundamental mode. Only the power output in the fundamental mode is measured, such that inter-modal mixing reflects in the transmission loss.

Bend type	**Samples**	**Transmission**		
		Mean	**Mean (dB)**	**Median (dB)**
Single mode	11	0.5 ± 0.2	-2.6	-2.9
Circular multimode	11	0.02 ± 0.01	-17	-17
Optimized multimode	25	0.6 ± 0.2	-2.5	-2.2

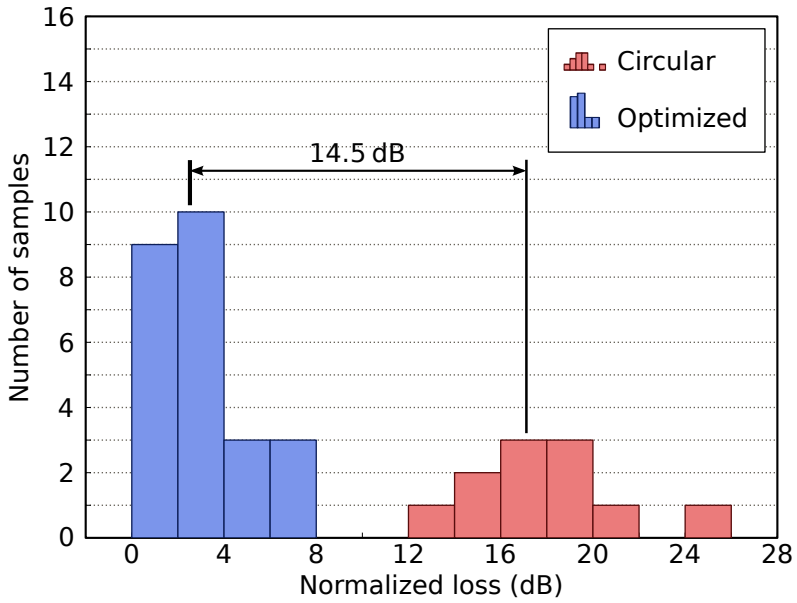

Figure 24 Histogram of the transmission loss for the circular and the optimized bends, reflecting the degree of excitation of higher order modes along them. The optimized GRIN bend shows a gain over the circular one by approximately 14.5 dB in average on the transmission of the fundamental mode.

5.4 Conclusions

In this chapter we demonstrated the power of TO in large-scale inverse design problems to enable multimode photonics on chip. Using our grayscale electron beam fabrication platform we show that routing signals in multimode silicon waveguides can be as efficient as on single mode waveguides, enabling the future possibility of modal multiplexing and ultra-high data rates.

Challenges in the fabrication of these structures are directly related to the sensitivity of the process to environmental and process conditions, including, as of now, the operator. These limitations are, nevertheless, not fundamental, and can be overcome with automation of the steps still conducted by hand, and possible development of low contrast resists for less

sensitive calibration curves.

The demonstrated bend is a first example of device using this design and fabrication platforms for multimode photonics, and already display efficiency on par with their single mode counterparts and far superior than circular multimode bends.

6 Concluding Remarks & Future Directions

The spread of TO and the progress in metamaterial theory and fabrication leveraged the growing interest of the scientific community in novel electromagnetic devices. From the original cloaking proposals to the research in super-resolution imaging, many ideas in the emerging field of complex media remain to be explored.

Our main objective within this work was to demonstrate the possibility of realizing complex devices and GRIN media in the optical domain, with special interest in integrated photonics. Integrated photonics remains one of the best candidates for future ultra-high data rate interconnects, and it is our belief that complex media can play an important role in enabling this technology to move from the optical table to the packaged product.

We started by reviewing the theory of TO and the field of metamaterials, as well as the strong connection between the two. The effort in bringing those ideas to optical frequencies faces two main challenges: natural materials offer a smaller variety of parameters than in

microwaves or RF, and nanostructured metamaterials require length scales not yet available through conventional fabrication processes. These issues result in additional constraints and compromises in the design of GRIN media, either by TO or any other method. The use of resonant metamaterials is usually followed by high losses, due to the poor characteristics of metals at optical frequencies. It also means more complex structures, making non-homogeneous media fabrication impossible as of now. By avoiding resonant responses we require that constitutive parameters lie in the range of naturally occurring values, which means that no magnetic materials can be used. Similar to resonant metamaterials, anisotropic dielectrics can be demonstrated, but non-homogeneous versions are still in very early development.

By choosing to constrain our designs to media defined by a non-homogeneous, isotropic refractive index distribution we are capable of implementing them using only dielectrics. We use planar devices, where the in-plane effective index plays the role of the designed index distribution. This way, we can freely control the propagation index by the geometry or effective material in our vertically confined slab waveguide. Three fabrication platforms were developed based on these control parameters for near infrared frequencies. They were demonstrated by implementing complex GRIN devices.

We first demonstrated optical invisibility cloaking by hiding a region of space from any external observer. The GRIN medium was composed of nanometer-size silicon pillars whose density is proportional to the local effective index. The main advantage of this platform is that it only employs conventional, well developed fabrication techniques. On the downside, the finite ratio between wavelength and nano-structure dimensions inevitably lead to scattering losses.

An alternative solution was proposed in the fabrication of a fiber-to-waveguide coupler mediated by a Luneburg lens, a GRIN aberration-free spherical lens. By directly sculpting the silicon surface with a FIB we vary the thickness of the slab waveguide and generate the required effective index distribution. With the small resulting surface roughness, scattering is well controlled. However, heavy ion implantation and damages to the crystalline structure of the silicon layer result in absorption in the GRIN material.

The Luneburg lens demonstration was also one of the first demonstrations of a complex device integrated with a conventional nanophotonic system, whereas thus far, most demonstrations involved standalone devices only. The addition of the lens results in a more robust fiber-to-waveguide coupler, decreasing its sensitivity to misalignments, and represents the first step in using GRIN devices to improve conventional photonic designs.

Continuing the development of a low loss platform for complex media and further integration with conventional nanophotonics, we proposed the use of grayscale electron beam lithography to pattern the silicon slab in the same way as we did using the FIB. The main challenge in this process is the requirement of careful calibration and characterization of each fabrication step. Once that is done, low surface roughness and low losses can be obtained.

This platform was used to demonstrate the possibility of routing an optical signal in a multimode waveguide without mode conversion. We designed and optimized a multimode bend based on TO with minimal modal mixing, indicating the possibility of using modal multiplexing in future optical communication channels along with wavelength multiplexing, increasing their transmission data rates by folds. The insertion loss of our multimode bend for the fundamental mode was the same as the insertion loss for a single mode bend.

Many possibilities are left as continuations of this work. Research in modal multiplexing is progressing fast in free-space and fiber optics, so it is natural that integrated photonics should follow in the same direction. But the optimization process developed for multimode photonics can also benefit other areas, in special non-linear optics, since the designed devices preserve not only the mode shapes, but also their relative phase, enabling phase-matched processes in mutimode devices—an additional degree of freedom for dispersion engineering. Multimode resonators is another direct path of research that follows the development of multimode waveguides, working as add-drop filters for modes, in analogy to the ones for wavelengths.

Of course, many improvements are still necessary in the fabrication process itself. Use of local oxidation techniques to decrease surface roughness or completely define the effective GRIN medium are promising ideas, as well as working with SiON films to vary both the material index and thickness simultaneously. Other material platforms could also be interesting, such as SiC to enable the use of anisotropy, or AlN for electro-optic control of adaptive GRIN devices.

In all, the field of complex materials, and in particular GRIN media, has just now started to be explored, and still holds many opportunities for novel research, either in fabrication techniques, devices, or basic electromagnetic effects. We believe that our work is an important part in enabling these new ideas, allowing for the continued progress of complex devices in the optical domain.

References

[1] S. E. Miller, *Light Propagation in Generalized Lens-Like Media*, Bell System Technical Journal **44** (1965), no. 9, 2017–2064

[2] S. Kawakami and J.-I. Nishizawa, *An Optical Waveguide with the Optimum Distribution of the Refractive Index with Reference to Waveform Distortion*, IEEE Transactions on Microwave Theory and Techniques **16** (1968), no. 10, 814–818

[3] T. Uchida *et al.*, *A light-focusing fiber guide*, IEEE Journal of Quantum Electronics **5** (1969), no. 6, 331–331

[4] T. Uchida *et al.*, *Optical characteristics of a light-focusing fiber guide and its applications*, IEEE Journal of Quantum Electronics **6** (1970), no. 10, 606–612

[5] M. S. Sodha, A. K. Ghatak, and D. P. S. Malik, *Electromagnetic Wave Propagation in Radially and Axially Nonuniform Media: Geometrical-Optics Approximation*, Journal of the Optical Society of America **61** (1971), no. 11, 1492

[6] K. Koizumi *et al.*, *New Light-Focusing Fibers Made by a Continuous Process*, Applied Optics **13** (1974), no. 2, 255

[7] E. G. Rawson, D. R. Herriott, and J. McKenna, *Analysis of Refractive Index Distributions in Cylindrical, Graded-Index Glass Rods (GRIN Rods) Used as Image Relays*, Applied Optics **9** (1970), no. 3, 753–759

[8] R. Ulrich and R. J. Martin, *Geometrical Optics in Thin Film Light Guides*, Applied Optics **10** (1971), no. 9, 2077

[9] F. Zernike, *Luneburg lens for optical waveguide use*, Optics Communications **12** (1974), no. 4, 379–381

[10] B.-U. Chen, E. Marom, and A. Lee, *Geodesic lenses in single-mode LiNbO3 waveguides*, Applied Physics Letters **31** (1977), no. 4, 263

[11] A. J. Ward and J. B. Pendry, *Refraction and geometry in Maxwell's equations*, Journal of Modern Optics **43** (1996), no. 4, 773–793

[12] R. K. Luneburg, *Mathematical Theory of Optics*. (University of California Press, 1964).

[13] M. Lax and D. Nelson, *Maxwell equations in material form*, Physical Review B **13** (1976), no. 4, 1777–1784

[14] U. Leonhardt, *Optical conformal mapping*, Science **312** (2006), no. 5781, 1777–80

[15] U. Leonhardt and T. G. Philbin, *General relativity in electrical engineering*, New Journal of Physics **8** (2006), no. 10, 247

[16] J. B. Pendry, D. Schurig, and D. R. Smith, *Controlling Electromagnetic Fields*, Science **312** (2006), no. 23, 1780–1782

[17] D. Schurig, J. B. Pendry, and D. R. Smith, *Calculation of material properties and ray tracing in transformation media*, Optics Express **14** (2006), no. 21, 9794

[18] F. Xu *et al.*, *Fabrication, modeling, and characterization of form-birefringent nanostructures*, Optics Letters **20** (1995), no. 24, 2457

[19] D. Smith, J. Mock, A. Starr, and D. Schurig, *Gradient index metamaterials*, Physical Review E **71** (2005), no. 3, 036609

[20] R. B. Greegor *et al.*, *Simulation and testing of a graded negative index of refraction lens*, Applied Physics Letters **87** (2005), no. 9, 091114

[21] A. Alù and N. Engheta, *Achieving transparency with plasmonic and metamaterial coatings*, Physical Review E **72** (2005), no. 1, 16623

[22] T. Driscoll *et al.*, *Free-space microwave focusing by a negative-index gradient lens*, Applied Physics Letters **88** (2006), no. 8, 081101

[23] V. M. Shalaev, *Physics: Transforming light*, Science **322** (2008), no. 5900, 384–6

[24] U. Leonhardt and T. G. Philbin, Transformation Optics and the Geometry of Light, in *Progress in Optics*, edited by E. Wolf , number 53 in Progress in Optics, chapter 2 (Elsevier), p. 69–152.

[25] U. Leonhardt and T. Philbin, *Geometry and Light: The Science of Invisibility.* (Dover Publications, 2010).

[26] J. Pendry, A. Holden, D. Robbins, and W. Stewart, *Magnetism from conductors and enhanced nonlinear phenomena*, IEEE Transactions on Microwave Theory and Techniques **47** (1999), no. 11, 2075–2084

[27] V. G. Veselago, *The electrodynamics of substances with simultaneously negative values of ϵ and μ*, Soviet Physics Uspekhi **10** (1968), no. 4, 509–514

[28] D. R. Smith *et al.*, *Composite Medium with Simultaneously Negative Permeability and Permittivity*, Physical Review Letters **84** (2000), no. 18, 4184–4187

[29] R. A. Shelby, D. R. Smith, and S. Schultz, *Experimental verification of a negative index of refraction.*, Science (New York, N.Y.) **292** (2001), no. 5514, 77–9

[30] C. Parazzoli *et al.*, *Experimental Verification and Simulation of Negative Index of Refraction Using Snell's Law*, Physical Review Letters **90** (2003), no. 10, 107401

[31] A. Houck, J. Brock, and I. Chuang, *Experimental Observations of a Left-Handed Material That Obeys Snell's Law*, Physical Review Letters **90** (2003), no. 13, 137401

[32] N. Engheta, *An idea for thin subwavelength cavity resonators using metamaterials with negative permittivity and permeability*, Antennas and Wireless Propagation Letters **1** (2002), no. 1, 10–13

[33] A. Alù and N. Engheta, *Pairing an epsilon-negative slab with a mu-negative slab: Resonance, tunneling and transparency*, IEEE Transactions on Antennas and Propagation **51** (2003), no. 10, 2558–2571

[34] A. Alù and N. Engheta, *Guided Modes in a Waveguide Filled With a Pair of Single-Negative (SNG), Double-Negative (DNG), and/or Double-Positive (DPS) Layers*, IEEE Transactions on Microwave Theory and Techniques **52** (2004), no. 1, 199–210

[35] N. Engheta, A. Salandrino, and A. Alù, *Circuit Elements at Optical Frequencies: Nanoinductors, Nanocapacitors, and Nanoresistors*, Physical Review Letters **95** (2005), no. 9, 95504

[36] N. Engheta, *Circuits with light at nanoscales: optical nanocircuits inspired by metamaterials*, Science **317** (2007), no. 5845, 1698–702

[37] A. Alù, A. Salandrino, and N. Engheta, *Coupling of optical lumped nanocircuit elements and effects of substrates*, Optics Express **15** (2007), no. 21, 13865

[38] M. G. Silveirinha, A. Alù, J. Li, and N. Engheta, *Nanoinsulators and nanoconnectors for optical nanocircuits*, Journal of Applied Physics **103** (2008), no. 6, 064305

[39] J. B. Pendry, *Negative Refraction Makes a Perfect Lens*, Physical Review Letters **85** (2000), no. 18, 3966–3969

[40] W. Cai, D. Genov, and V. Shalaev, *Superlens based on metal-dielectric composites*, Physical Review B **72** (2005), no. 19, 193101

[41] N. Fang, H. Lee, C. Sun, and X. Zhang, *Sub-diffraction-limited optical imaging with a silver superlens*, Science **308** (2005), no. 5721, 534–7

[42] A. Salandrino and N. Engheta, *Far-field subdiffraction optical microscopy using metamaterial crystals: Theory and simulations*, Physical Review B **74** (2006), no. 7, 75103–75105

[43] S. Kawata, Y. Inouye, and P. Verma, *Plasmonics for near-field nano-imaging and superlensing*, Nat Photon **3** (2009), no. 7, 388–394

[44] W. Cai, U. K. Chettiar, A. V. Kildishev, and V. M. Shalaev, *Optical cloaking with metamaterials*, Nat Photon **1** (2007), no. 23, 224–227

[45] D. Schurig *et al.*, *Metamaterial Electromagnetic Cloak at Microwave Frequencies*, Science **314** (2006), no. 23, 977–980

[46] D. A. Roberts, M. Rahm, J. B. Pendry, and D. R. Smith, *Transformation-optical design of sharp waveguide bends and corners*, Applied Physics Letters **93** (2008), no. 25, 251111

[47] H. Chen, C. T. Chan, and P. Sheng, *Transformation optics and metamaterials*, Nature Materials **9** (2010), no. 5, 387–96

[48] N. Liu *et al.*, *Three-dimensional photonic metamaterials at optical frequencies*, Nature materials **7** (2008), no. 1, 31–7

[49] M. S. Rill *et al.*, *Photonic metamaterials by direct laser writing and silver chemical vapour deposition.*, Nature materials **7** (2008), no. 7, 543–6

[50] M. Thiel, M. Wegener, and G. von Freymann *Three-dimensional chiral photonic crystals by direct laser writing*, in *Proceedings of SPIE* (SPIE, 2008), pp. 68830K–68830K–6.

[51] M. D. Turner, G. E. Schröder-Turk, and M. Gu, *Fabrication and characterization of three-dimensional biomimetic chiral composites*, Optics Express **19** (2011), no. 10, 10001

[52] C. M. Soukoulis and M. Wegener, *Past achievements and future challenges in the development of three-dimensional photonic metamaterials*, Nature Photonics **5** (2011), no. 9, 523–530

[53] J. Li and J. B. Pendry, *Hiding under the Carpet: A New Strategy for Cloaking*, Physical Review Letters **101** (2008), no. 20, 203901–203904

[54] L. H. Gabrielli and M. Lipson, *Transformation optics on a silicon platform*, Journal of Optics **13** (2011), no. 2, 024010

[55] A. E. T. Kuiper, *Deposition and composition of silicon oxynitride films*, Journal of Vacuum Science & Technology B: Microelectronics and Nanometer Structures **1** (1983), no. 1, 62

[56] P. G. Snyder, *Graded refractive index silicon oxynitride thin film characterized by spectroscopic ellipsometry*, Journal of Vacuum Science & Technology A: Vacuum, Surfaces, and Films **10** (1992), no. 4, 1462

[57] R. de Ridder *et al.*, *Silicon oxynitride planar waveguiding structures for application in optical communication*, IEEE Journal of Selected Topics in Quantum Electronics **4** (1998), no. 6, 930–937

[58] T. Nakamura, M. Shimizu, H. Kimura, and R. Sato, *Effective permittivity of amorphous mixed materials*, Electronics and Communications in Japan (Part I: Communications) **88** (2005), no. 10, 1–9

[59] R. W. Floyd and L. Steinberg, *An Adaptive Algorithm for Spatial Greyscale*, Proceedings of the Society for Information Display **17** (1976), no. 2, 75–77

[60] S. K. Yao *et al.*, *Guided-wave optical thin-film Luneburg lenses: fabrication technique and properties*, Applied Optics **18** (1979), no. 24, 4067

[61] J. Brazas, G. Kohnke, and J. McMullen, *Mode-Index Waveguide Lens With Novel Gradient Boundaries Developed For Application To Optical Recording*, Applied Optics **31** (1992), no. 18, 3420

[62] M.-C. Lee and M. Wu, *Thermal Annealing in Hydrogen for 3-D Profile Transformation on Silicon-on-Insulator and Sidewall Roughness Reduction*, Journal of Microelectromechanical Systems **15** (2006), no. 2, 338–343

[63] A. Di Falco, S. C. Kehr, and U. Leonhardt, *Luneburg lens in silicon photonics*, Optics Express **19** (2011), no. 6, 5156

[64] J. Kim, D. Joy, and S.-Y. Lee, *Controlling resist thickness and etch depth for fabrication of 3D structures in electron-beam grayscale lithography*, Microelectronic Engineering **84** (2007), no. 12, 2859–2864

[65] L. Mosher, C. M. Waits, B. Morgan, and R. Ghodssi, *Double-Exposure Grayscale Photolithography*, Journal of Microelectromechanical Systems **18** (2009), no. 2, 308–315

[66] R. Murali, D. K. Brown, K. P. Martin, and J. D. Meindl, *Process optimization and proximity effect correction for gray scale e-beam lithography*, Journal of Vacuum Science & Technology B: Microelectronics and Nanometer Structures **24** (2006), no. 6, 2936

[67] D. A. B. Miller, *On perfect cloaking*, Optics Express **14** (2006), no. 25, 12457

[68] Y. Huang, Y. Feng, and T. Jiang, *Electromagnetic cloaking by layered structure of homogeneous isotropic materials*, Optics Express **15** (2007), no. 18, 11133

[69] W. Cai *et al.*, *Nonmagnetic cloak with minimized scattering*, Applied Physics Letters **91** (2007), no. 11, 111105

[70] M. G. Silveirinha, A. Alù, and N. Engheta, *Parallel-plate metamaterials for cloaking structures*, Physical Review E **75** (2007), no. 3, 36603–36616

[71] W. X. Jiang *et al.*, *Analytical design of conformally invisible cloaks for arbitrarily shaped objects*, Physical Review E **77** (2008), no. 6, 66606–66607

[72] A. Alù and N. Engheta, *Multifrequency Optical Invisibility Cloak with Layered Plasmonic Shells*, Physical Review Letters **100** (2008), no. 11, 113901–113904

[73] I. I. Smolyaninov, Y. J. Hung, and C. C. Davis, *Two-dimensional metamaterial structure exhibiting reduced visibility at 500 nm*, Optics Letters **33** (2008), no. 12, 1342

[74] W. Li, J. Guan, Z. Sun, and W. Wang, *Shifting cloaks constructed with homogeneous materials*, Computational Materials Science **50** (2010), no. 2, 607–611

[75] T. Tyc and U. Leonhardt, *Transmutation of singularities in optical instruments*, New Journal of Physics **10** (2008), no. 11, 115038

[76] U. Leonhardt and T. Tyc, *Broadband invisibility by non-Euclidean cloaking*, Science **323** (2009), no. 5910, 110–2

[77] Z. Ruan, M. Yan, C. W. Neff, and M. Qiu, *Ideal Cylindrical Cloak: Perfect but Sensitive to Tiny Perturbations*, Physical Review Letters **99** (2007), no. 11, 113903–113904

[78] L. H. Gabrielli, J. Cardenas, C. B. Poitras, and M. Lipson, *Silicon nanostructure cloak operating at optical frequencies*, Nature Photonics **3** (2009), no. 8, 461–463

[79] L. H. Gabrielli, J. Cardenas, C. B. Poitras, and M. Lipson *Demonstration of Cloaking at Optical Frequencies*, in *Conference on Lasers and Electro-Optics/International Quantum Electronics Conference, OSA Technical Digest (CD)* (Optical Society of America, 2009), p. IPDB3.

[80] J. Valentine *et al.*, *An optical cloak made of dielectrics*, Nature Materials **8** (2009), no. 7, 568–71

[81] R. Liu *et al.*, *Broadband ground-plane cloak*, Science **323** (2009), no. 5912, 366–9

[82] A. F. Oskooi *et al.*, *Meep: A flexible free-software package for electromagnetic simulations by the FDTD method*, Computer Physics Communications **181** (2010), no. 3, 687–702

[83] D. H. Spadoti, L. H. Gabrielli, C. B. Poitras, and M. Lipson, *Focusing light in a curved-space*, Optics Express **18** (2010), no. 3, 3181

[84] D. H. Spadoti, L. H. Gabrielli, C. B. Poitras, and M. Lipson *Focusing Light in a Curved-Space*, in *Quantum Electronics and Laser Science Conference, OSA Technical Digest (CD)* (Optical Society of America, 2010), p. JWA1.

[85] L. H. Gabrielli and M. Lipson, *Integrated Luneburg lens via ultra-strong index gradient on silicon*, Optics Express **19** (2011), no. 21, 20122

[86] L. H. Gabrielli and M. Lipson *Integrated Gradient Index Luneburg Lens for Robust Fiber-to-Chip Coupling*, in *CLEO: QELS-Fundamental Science, OSA Technical Digest* (Optical Society of America, 2012), p. QM1C.1.

[87] T. Shoji *et al.*, *Low loss mode size converter from 0.3 [micro sign]m square Si wire waveguides to singlemode fibres*, Electronics Letters **38** (2002), no. 25, 1669

[88] V. R. Almeida, R. R. Panepucci, and M. Lipson, *Nanotaper for compact mode conversion*, Optics Letters **28** (2003), no. 15, 1302

[89] K. K. Lee *et al.*, *Mode transformer for miniaturized optical circuits*, Optics Letters **30** (2005), no. 5, 498

[90] G. Roelkens *et al.*, *Efficient silicon-on-insulator fiber coupler fabricated using 248-nm-deep UV lithography*, IEEE Photonics Technology Letters **17** (2005), no. 12, 2613–2615

[91] G. P. Agrawal, *Fiber-optic communication systems*. (Wiley, 1997), 2nd ed.

[92] A. Logg, K.-A. Mardal, and G. Wells, editors, *Automated Solution of Differential Equations by the Finite Element Method* Number 84 in Lecture Notes in Computational Science and Engineering. (Springer Berlin Heidelberg, Berlin, Heidelberg, 2012).

[93] L. H. Gabrielli, D. Liu, S. G. Johnson, and M. Lipson *On-Chip Multimode Photonics*, in *CLEO: QELS-Fundamental Science, OSA Technical Digest* (Optical Society of America, 2012), p. QTh5B.4.

[94] R. Waldhäusl *et al.*, *Efficient coupling into polymer waveguides by gratings*, Applied optics **36** (1997), no. 36, 9383–90

[95] D. Taillaert, P. Bienstman, and R. Baets, *Compact efficient broadband grating coupler for silicon-on-insulator waveguides*, Optics Letters **29** (2004), no. 23, 2749

[96] D. Taillaert *et al.*, *Grating Couplers for Coupling between Optical Fibers and Nanophotonic Waveguides*, Japanese Journal of Applied Physics **45** (2006), no. No. 8A, 6071–6077

[97] F. Van Laere *et al.*, *Compact focusing grating couplers for silicon-on-insulator integrated circuits*, Photonics Technology Letters, IEEE **19** (2007), no. 23, 1919–1921